REPORT DOCUMENTATION PAGE

Form Approved OMB NO. 0704-0188

1. REPORT DATE (DD-MM-YYYY)	2. REPORT TYPE	3. DATES COVERED (From - To)
06-07-2021	Final Report	1-Jun-2019 - 28-Feb-2021

4. TITLE AND SUBTITLE
Final Report: Quantum Theory and Measured Turnover Rates: Perovskite Chemical Transistors for Non-Faradaic Alkane Isomerization

5a. CONTRACT NUMBER
W911NF-19-1-0318

5b. GRANT NUMBER

5c. PROGRAM ELEMENT NUMBER
611104

6. AUTHORS

5d. PROJECT NUMBER

5e. TASK NUMBER

5f. WORK UNIT NUMBER

7. PERFORMING ORGANIZATION NAMES AND ADDRESSES
Northeastern University
360 Huntington Avenue
490 RP
Boston, MA 02115 -5005

8. PERFORMING ORGANIZATION REPORT NUMBER

9. SPONSORING/MONITORING AGENCY NAME(S) AND ADDRESS (ES)
U.S. Army Research Office
P.O. Box 12211
Research Triangle Park, NC 27709-2211

10. SPONSOR/MONITOR'S ACRONYM(S)
ARO

11. SPONSOR/MONITOR'S REPORT NUMBER(S)
75281-CH-II.3

12. DISTRIBUTION AVAILIBILITY STATEMENT
Approved for public release; distribution is unlimited.

13. SUPPLEMENTARY NOTES
The views, opinions and/or findings contained in this report are those of the author(s) and should not contrued as an official Department of the Army position, policy or decision, unless so designated by other documentation.

14. ABSTRACT

15. SUBJECT TERMS

16. SECURITY CLASSIFICATION OF:			17. LIMITATION OF ABSTRACT	15. NUMBER OF PAGES	19a. NAME OF RESPONSIBLE PERSON
a. REPORT	b. ABSTRACT	c. THIS PAGE			Eugene Smotkin
UU	UU	UU	UU		19b. TELEPHONE NUMBER 617-373-7526

RPPR Final Report
as of 12-Jul-2021

Agency Code: 21XD

Proposal Number: 75281CHII **Agreement Number: W911NF-19-1-0318**
INVESTIGATOR(S):

Name: Eugene Smotkin
Email: e.smotkin@northeastern.edu
Phone Number: 6173737526
Principal: Y

Organization: **Northeastern University**
Address: 360 Huntington Avenue, Boston, MA 021155005
Country: USA
DUNS Number: 001423631 EIN: 104167998

Report Date: 31-May-2021 Date Received: 06-Jul-2021

Final Report for Period Beginning 01-Jun-2019 and Ending 28-Feb-2021
Title: Quantum Theory and Measured Turnover Rates: Perovskite Chemical Transistors for Non-Faradaic Alkane Isomerization
Begin Performance Period: 01-Jun-2019 **End Performance Period:** 28-Feb-2021
Report Term: 0-Other

Submitted By: Eugene Smotkin Email: e.smotkin@northeastern.edu
Phone: (617) 373-7526

Distribution Statement: 1-Approved for public release; distribution is unlimited.

STEM Degrees: 1 **STEM Participants:** 4

Major Goals: 1) Fabricate compacted yttrium-doped barium cerate perovskite discs for use as electrolytes in an electrochemical reactor.
2) Assemble proton conducting perovskite-based chemical transistors for methylcyclohexane (MCH) isomerization.
3) Measure MCH isomerization rates vs. potential at 200 - 325 °C by GC-MS
4) Characterize the transistor collector-emitter surface by operando IR/Raman spectroscopy.
5) Use DFT for both normal mode analyses for vibrational spectroscopy and electron density topological analyses by QTAIM.

Development of an electrochemical reactor that could readily incorporate free-standing perovskite electrolytes proved to be a more time-intensive development process than initially presumed. The initial prototype caused difficulties with consistent assembly (only functioning properly when the electrolyte, GDLs for anode and cathode, and associated o-rings were placed in the perfect positions). A few revised reactor designs were either too fragile or leaked. Eventually, a robust and reliable electrochemical cell was constructed.

Because each iteration of the new electrochemical reactor took time to design, manufacture, and test, significant effort was placed into open circuit studies of MCH modification--namely, dehydrogenation to toluene. Using our high-throughput MIMS system, we were able to probe MCH dehydrogenation over a bead-based Pt-loaded solid oxide. The results from this, combined with other recent insights on MCH dehydrogenation posited in the literature, permitted us to propose an experiment-guided mechanistic breakdown for MCH conversion to toluene.

Accomplishments: A detailed overview of our accomplishments under this grant performance period can be found in the attached "Upload" document. The information therein regarding our findings for the high-throughput laser-activated membrane introduction mass spectrometry evaluation of open circuit MCH modification can also be found in Kim, R. Y. et al., "A Laser-Activated Membrane Introduction Mass Spectrometry Study of Proton Spillover Promoted Alkane Dehydrogenation." Anal. Chem., 2020, 92, 13462-13469.

Our persistent and extensive efforts in designing a new high temperature electrochemical reactor manifold, designed to permit the use of a disc-style doped perovskite electrolyte at 200 - 325 °C, ultimately resulted in fabrication of a completely leak-proof, fully operational fuel cell-style reactor. This reactor now permits us to pursue the MCH isomerization distribution sought in our original proposal. Standards of all available MCH isomers have already been characterized by GC with respect to retention times and optimized run conditions.

Modification of the finalized electrochemical cell for use as an operando IR/Raman medium is underway, and computational studies (including DFT and QTAIM) are still planned for probing proton trajectory in the electrolyte as well as proton-reagent interaction at the catalyst surface.

Finally, analysis of our proton spillover-mediated hydrocarbon modification reactions driven by electrochemical means as well as by dihydrogen partial pressures enabled us to submit a manuscript on electrochemically controlled (EC) and molecular hydrogen originated (MHO) protonics, submitted to Catalysis Today as a follow up to our presentation on this topic at the 5th International Conference on Catalysis and Chemical Engineering. The article, submitted to Catalysis Today, is Smith, S. J. et al., "Bridging the gap between electrochemical and molecular hydrogen-originated surface protonics for acid catalyzed petrochemical reactions." Catal. Today, submitted.

Training Opportunities: Nothing to Report

Results Dissemination: Results from open circuit studies of high-throughput MCH modification over bead catalysts obtained during this grant program have been published in Kim, R. Y. et al., "A Laser-Activated Membrane Introduction Mass Spectrometry Study of Proton Spillover Promoted Alkane Dehydrogenation." Anal. Chem., 2020, 92, 13462-13469. Additionally, insight gained from studies carried out during this program have been submitted to Catalysis Today as Smith, S. J. et al., "Bridging the gap between electrochemical and molecular hydrogen-originated surface protonics for acid catalyzed petrochemical reactions." Catal. Today, submitted.

Honors and Awards: Nothing to Report

Protocol Activity Status:

Technology Transfer: Nothing to Report

PARTICIPANTS:

Participant Type: PD/PI
Participant: Eugene S. Smotkin
Person Months Worked: 15.00 **Funding Support:**
Project Contribution:
National Academy Member: N

Participant Type: Graduate Student (research assistant)
Participant: Sam Jackson Smith
Person Months Worked: 15.00 **Funding Support:**
Project Contribution:
National Academy Member: N

Participant Type: Graduate Student (research assistant)
Participant: Ryan Cruse
Person Months Worked: 12.00 **Funding Support:**
Project Contribution:
National Academy Member: N

Participant Type: Undergraduate Student
Participant: Kyra Perz
Person Months Worked: 9.00 **Funding Support:**
Project Contribution:

RPPR Final Report
as of 12-Jul-2021

National Academy Member: N

Participant Type: Undergraduate Student
Participant: Katrina Ipser
Person Months Worked: 3.00 **Funding Support:**
Project Contribution:
National Academy Member: N

Partners

,

Carlo Segre (Illinois Institute of Technology, IL, USA)Richard R. Willis (UOP LLC, a Honeywell Company, IL, USA)D

I certify that the information in the report is complete and accurate:
Signature: Eugene Smotkin
Signature Date: 7/6/21 6:21PM

Final Report

Short-Term Innovative Research (STIR) Program

Quantum Theory and Measured Turnover Rates: Perovskite Chemical Transistors for Non-Faradaic Alkane Isomerization

W911NF-19-1-0318

Start Date: 06/01/2019

End Date (Revised as of 05/08/2020): 02/28/2021

Northeastern University

Organization's Unique Entity Identifier: 001423631

Eugene S. Smotkin

Abstract

This final report describes work performed toward the development of a pelletized proton-conducting perovskite electrolyte for use in an electrochemical reactor system aimed at isomerizing alkanes via potential-controlled proton spillover. The intent of the initial proposal was to develop a reliable synthetic procedure for creating $BaCe_{1-x}Y_xO_{3-\delta}$ pellets, using powder XRD and vibrational spectroscopy to analyze perovskite samples, creating an electrochemical reactor system for analyzing methylcyclohexane turnover, and performing computational studies to probe proton trajectory in proton-conducting perovskites. In what follows, a brief overview of studies on the non-Faradaic electrochemical modification of catalytic activity (NEMCA) is provided for context of our experiment. A short discussion on how we posit that the NEMCA effect will be observable for alkane (i.e., methylcyclohexane) isomerization in an electrochemical system at elevated temperatures using solid oxide proton conductor electrolytes is also included. Results of the perovskite synthesis and characterization as well as progress on the reactor system are then recounted before elaborating on continued efforts and future work to be pursued in the coming weeks and months.

Non-Faradaic Electrochemical Modification of Catalytic Activity (NEMCA)

The term for the effect of non-faradaic electrochemical modification of catalytic activity (i.e., the NEMCA effect) was originally coined by Vayenas, Bebelis, and Neophytides during their study of ethylene and methanol decomposition at the surface of a potential-controlled metal-coated solid oxide electrolyte.[1] Enhancement (Λ) of the change in rate of a catalytic reaction (Δr) had already been established as being proportional to Faraday's constant (F) by equation (1). Increase in reaction rate was proportional to the rate at which oxide ions in a metal-coated solid oxide electrolyte were pumped to the surface where heterogeneous reactions occurred. However, this group found that upon applying a constant current to the electrolyte species, reaction rates up to an order of magnitude greater than at open circuit voltage (corresponding to an enhancement factor, Λ, of ~15,000) were achieved. This supports that for every oxide ion brought to the catalytic surface, 15,000 chemisorbed oxygens reacted with the reagent gases. The equation for Λ was then modified to (2) in order to reflect the importance of having low exchange current (the product of electrode area, A, and exchange current density, i_o) and high intrinsic catalytic rate (r_o) in order to facilitate the NEMCA effect. Increase in catalytic activity, and consequent decrease in reaction activation energy, was ultimately attributed to the accumulation of negative charge as oxide ions accrue at the catalytic surface. This charge accumulation was found to increase work function of the metal catalyst clusters on the oxide surface, and this work function was discovered to increase or decrease upon application of positive or negative currents, respectively.[2-3]

$$\Lambda = \frac{\Delta r}{\left(\frac{i}{2F}\right)} \tag{1}$$

$$\Lambda \approx \frac{2Fr_o}{Ai_o} \tag{2}$$

Other NEMCA studies have sought to gain further understanding of this effect by using similar solid oxides to study total propene oxidation,[4-5] by investigating effects of using mixed ionic-electronic solid electrolytes,[6] and by analyzing the effect of catalytic Pt cluster size on rate enhancement.[7] Our group's examination of the NEMCA effect is unique in that we observed rate enhancement of non-redox catalytic reactions (1-butene isomerization and reduction) via proton

spillover through a Nafion 117 electrolyte onto a Pd surface.[8] Subsequent study[9] with oxidation of D_2 at the anode of our cell permitted flux of D^+ through the Nafion, which facilitated Markovnikov additions to the 1-butene that ultimately resulted in desorbed species with unique isotope labels and fragments. These products were readily separated by a GC and subsequently analyzed by mass spectrometry to enable determination of the reaction mechanism (Fig. 1). In addition to unveiling the isomerization mechanism, this experiment showed that enhancement factor and product distribution were variable dependent upon the applied potential. This supports a clear NEMCA effect whereby more than one isomerization reaction could proceed for each proton electromigrated to the catalytic surface at the cathode.

Investigation of this effect using a 3,3-dimethyl-1-butene[10] not only revealed the same potential-dependent enhancement factor and product distribution (Fig. 2), but even revealed a more substantial product: the product of a methyl shift, 2,3-dimethylbutane. Given the need to overcome a larger activation barrier to achieve this product of skeletal rearrangement, this provided us encouragement that the same cell setup could be used to probe the NEMCA effect for higher energy alkane isomerization as well.

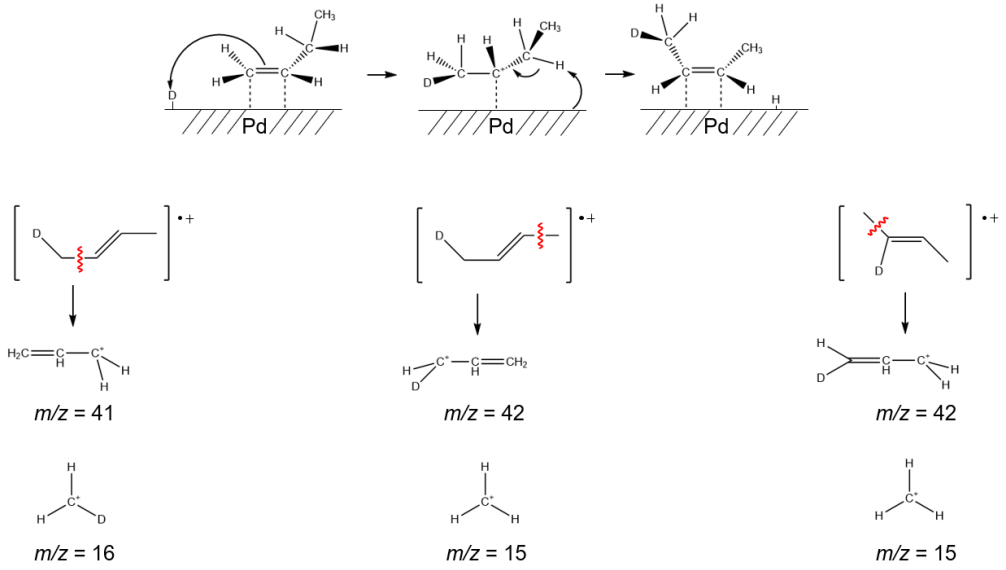

Figure 1. Top: isomerization mechanism of 1-butene at a Pd catalytic surface on a Nafion electrolyte, facilitated by spillover deuterium. Bottom: unique fragmentation patterns of various isotope-labelled isomers. Figures adapted from Ploense et al.[9]

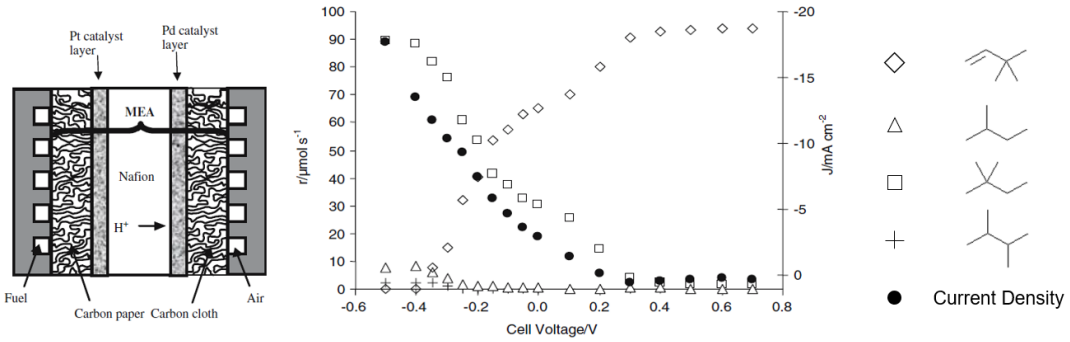

Figure 2. Setup of the electrochemical reactor (left) used in the analysis of potential-dependent product formation rate (middle) of the isomers and reduced products (right) generated from proton-promoted catalytic reaction of 2,3-dimethyl-1-butene. Figures adapted from Salazar et al.[10]

Proton-Promoted Alkane Isomerization

By exposing the cyclic alkane methylcyclohexane (MCH) to an array of Pt/zeolite catalysts at intermediate temperatures (200 – 325 °C), McVicker et al. at ExxonMobil were able to isomerize the MCH, yielding a distribution of ring-closing products that varied with catalyst acidity and pore size.[11] McVicker et al. proposed that the distribution of products was directly related to the stability of the transition state for each isomer. Their proposed transition species were non-classical carbocations, with the positive charge delocalized around a cyclopropyl moiety of the ring (Fig. 3). The more stable transition states were those that could place the positive charge on the tertiary carbon site or could place this charge on the adjacent secondary carbons. The group witnessed that Pt/zeolite catalysts with a smaller relative number of acid sites produced ethylcylopentane (ECP) to a quantifiably larger extent than catalysts with larger relative amounts of acid sites. Accordingly, it was suggested that catalysts with lower acid strength would interact with MCH to yield a larger proportion of ECP products, while catalysts with stronger acid sites (or a larger abundance of acid sites) would isomerize MCH to produce larger amounts of the isomers with less stable transition states.

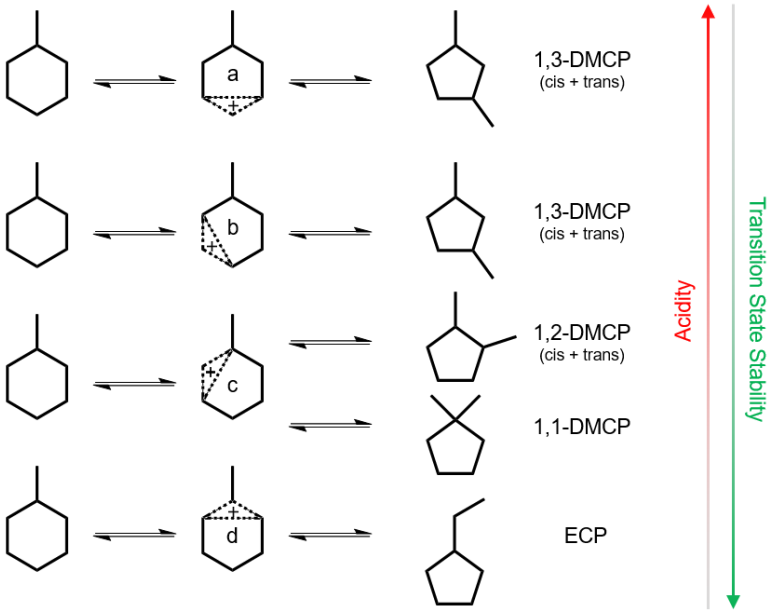

Figure 3. Non-classical carbocation transition states in the Pt/zeolite-catalyzed isomerization of methylcyclohexane (MCH). Relative stabilities of the transition states, along with the acid site strength expected to govern each product, is described by the arrows on the right. Product abbreviations are as follows: ethylcyclopentane (ECP), 1,2-dimethylcyclopentane (1,2-DMCP), 1,1-dimethylcyclopentane (1,1-DMCP), and 1,3-dimethylcylcopentane (1,3-DMCP). Figure is adapted from the work of McVicker et al.[11]

Given the similarity between the distributions of isomerized products observed by ExxonMobil based on acid strength compared with the distributions of isomers from 2,3-dimethyl-1-butene observed by our group resulting from varying applied potential, we selected methylcyclohexane

as a target reagent for attempting controlled isomerization of a fully saturated hydrocarbon in an electrochemical reactor. Successful control of isomer distribution at elevated temperatures by selecting the appropriate applied voltage would provide an unprecedented method of electrochemically generating alkane isomers that would otherwise be difficult to selectively produce.

Process Development for $BaCe_{1-x}Y_xO_{3-\delta}$ Discs

The synthesis of the $BaCe_{1-x}Y_xO_{3-\delta}$ (BCYx, where x is the molar percent of Y dopant) pellets proceeded by a previously reported sol-gel synthesis[12] followed by uniaxial pressing and sintering, as summarized in Figure 4. Nitrates of Ba, Ce, and Y in the desired molar ratios for a $BaCe_{1-x}Y_xO_{3-\delta}$ sample were dissolved in anhydrous ethylene glycol along with citric acid in a 2:1 molar ratio of citric acid to perovskite. This solution was stirred vigorously at 125 °C for 96 hours. The resulting viscous dark brown/black sol was collected in a ceramic crucible and calcined in an electric furnace at 800 °C for 12 hours, yielding a coarse off-white powder. This powder was ball milled using yttrium-stabilized zirconia (YSZ) and stainless-steel grinding media in 200 proof ethanol or anhydrous isopropyl alcohol for 24 hours. The milled mixture was strained through a stainless-steel sieve into a new ceramic crucible, and the captured slurry of solvent and powder was dried in a furnace. Powder was then delivered into a pressing die assembly along with 4 drops of 4 wt % poly(ethylene glycol) 400 in ethanol (200 proof). Uniaxial compaction[13] of the powder in stages—at 167 MPa, 251 MPa, and 301 MPa, for 10 minutes each—yielded uniform, disc-shaped pellets of BCYx. While testing effects of pressure on pellet stability, certain samples were pressed with a final pressure applied as high as 502 MPa. Each disc was coated on all faces with a thin layer of raw perovskite powder to prevent barium deposition from the surface during sintering,[14] after which all discs were loaded into a furnace to heat at 1 °C/min to 1100 °C with a hold time of 24 h before cooling also at 1 °C/min.

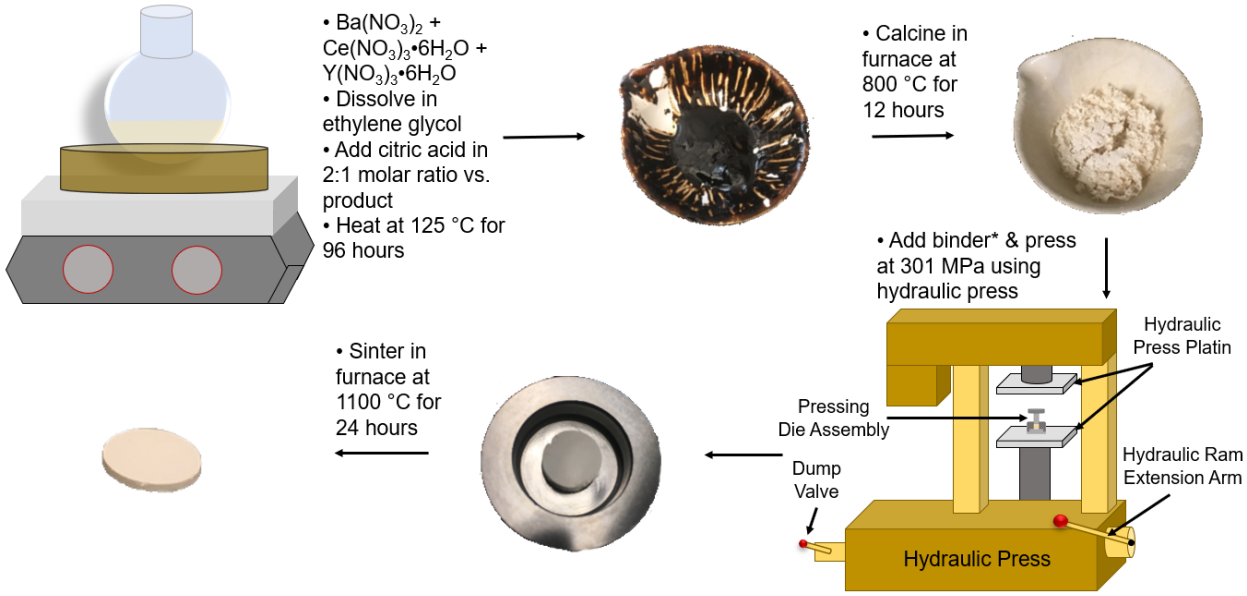

Figure 4. Overview of sol-gel synthesis along with the thermal and mechanical requirements for making a thin pelletized disc of $BaCe_{1-x}Y_xO_{3-\delta}$.

Characterization of $BaCe_{1-x}Y_xO_{3-\delta}$ Discs

Density

Perovskites discs prepared by the aforementioned synthesis were first inspected for visible cracks and imperfections. During the initial stages of process development for the samples, many contained small defects. Because density estimation by spatial dimensions and mass would be inaccurate for said samples, a density measurement apparatus (Fig. 5) was constructed in SolidWorks and 3D printed out of PLA. Measurement of the air and water temperature at the time each sample was massed in both air (top plate) and in solvent (hanging bottom plate) permitted calculation of the density by Archimedes' method (3).

$$\rho_{Disc} = \left(\frac{M_{Disc,air}}{M_{Disc,air} - M_{Disc,water}}\right) \times (\rho_{water} - \rho_{air}) + \rho_{air} \quad (3)$$

The first few samples studied with this apparatus were found to have densities ranging from 5.433 g/cm^3 to 5.602 g/cm^3 when measured using water as the solvent. This corresponds to 86% to 90% of theoretical density based on ionic radii. Surprisingly, samples without any defects were measured for mass and volume, which revealed densities ranging from approximately 3.5 g/cm^3 to 4.2 g/cm^3. Density measurements using the were then performed using the Archimedes' method apparatus for one singular disc, where the mass of the disc was obtained in air and then in a solvent, with the temperature of both recorded at the time of obtaining the mass. Deionized water, anhydrous isopropanol, and ethanol (200 proof) were used as the solvents, resulting in calculated densities for the single disc of 6.204 g/cm^3, 6.471 g/cm^3, and 4.722 g/cm^3, respectively. The disc was fully dried in an electric furnace between each density measurement. The inconsistency in the measurements attained using varied solvents may result from the ability of each to be absorbed into the perovskite lattice. Further investigation of gas permeation through the electrolyte discs using a submerged half-reactor setup did reveal gas leak through the electrolyte, suggesting a porosity that at least explains the low density calculations obtained using mass and volumetric measurements alone.

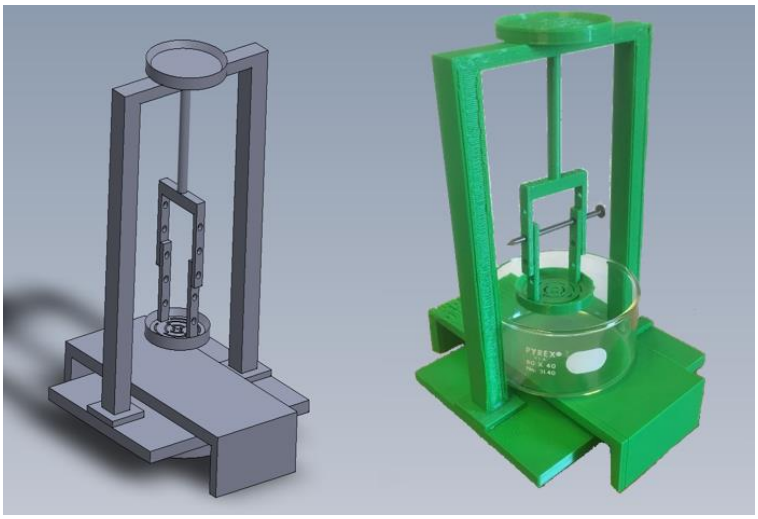

Figure 5. Density measurement apparatus as a SolidWorks concept (left) and as the fully 3D printed final product (right)

Powder X-Ray Diffraction

Powder XRD analysis of 6 separate $BaCe_{0.8}Y_{0.2}O_{3-\delta}$ (BCY20) discs resulted in an average pseudo-cubic lattice constant of 4.394040 Å ± 0.000639 Å. This was comparable to other reports of BCY20 X-ray data,[12, 15-18] but peak fitting for samples was not ideal. Furthermore, a preferrable orientation for each sample was difficult to locate, which could suggest phase-boundary formation or the existence of multiple cubic phases. Since pseudocubic lattice parameters differ from expected values,[19] further investigation of these structural inconsistencies is planned.

XRD data of a BCY20 perovskite sample prepared without the use of binder is demonstrated in Figure 6a, while a BCY20 disc compacted with 4 drops of 4 wt% poly(ethylene glycol) in ethanol (200 proof) added as binder is shown in Figure 6b. Peaks resulting from CeO_2 at $2\theta \approx 27$ and $BaCO_3$ at $2\theta \approx 34$, 42, and 45 are noticeably diminished for the sample to which binder was added prior to hydraulic pressing, so binder was added to all perovskite samples prepared following this XRD analysis.

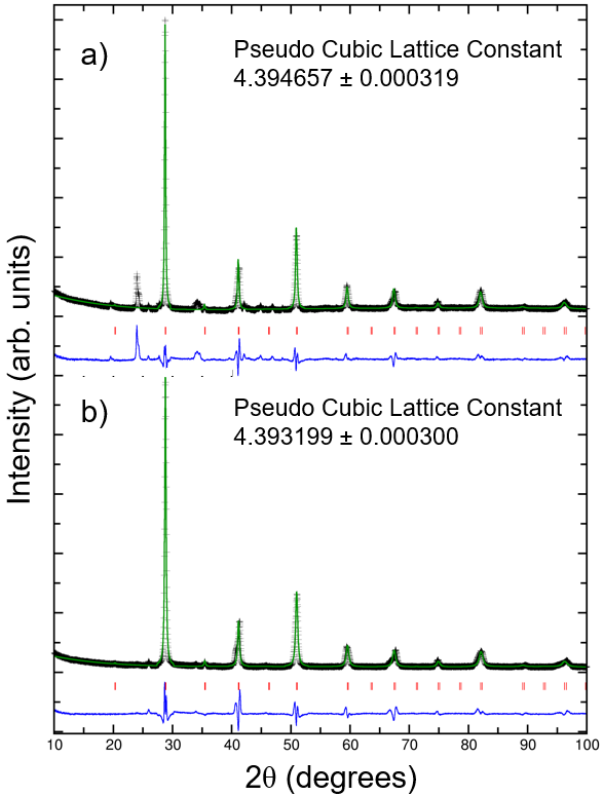

Figure 6. Powder X-ray diffraction spectra of $BaCe_{0.8}Y_{0.2}O_{3-\delta}$ (BCY20) prepared without the addition of binding agent (a), and with the addition of ~4 drops of 4 wt% PEG-400 in 200 proof ethanol (b).

Raman

Raman spectroscopy was used as the primary technique for evaluating structure and probing for impurities or defects in each perovskite disc. A 488 nm laser was used to acquire all spectra. Peaks at 461 cm^{-1}, ~890 cm^{-1}, and 1059 cm^{-1}, representative of CeO_2, Y_2O_3, and $BaCO_3$ impurities[20], respectively, were largely absent from Raman spectra for BCYx samples (Fig. 7) of three different concentrations (x = 15, 20, 25). At the same time, intense peaks typical of the

perovskite O-Ce-O bend[15, 17] appeared between 300-400 cm^{-1}, while the peak at 630 cm^{-1} can most likely be attributed to the dopant interactions (Y-O stretch).[21] The relative low intensity of the $BaCO_3$ peak suggests that exposure of these samples to H_2O during synthesis and subsequent exposure to atmospheric water vapor after synthesis was minimized,[22-23] which is important since proton conductor perovskites are known to degrade to form $BaCO_3$ and $Ba(OH)_2$ upon sustained exposure to H_2O.[24] Furthermore, the overall lack of CeO_2 peak at 461 cm^{-1} may help reinforce that barium was not lost from the surface during sintering due to the use of the raw powder coating over the pressed disc as the sample was sintered.[14]

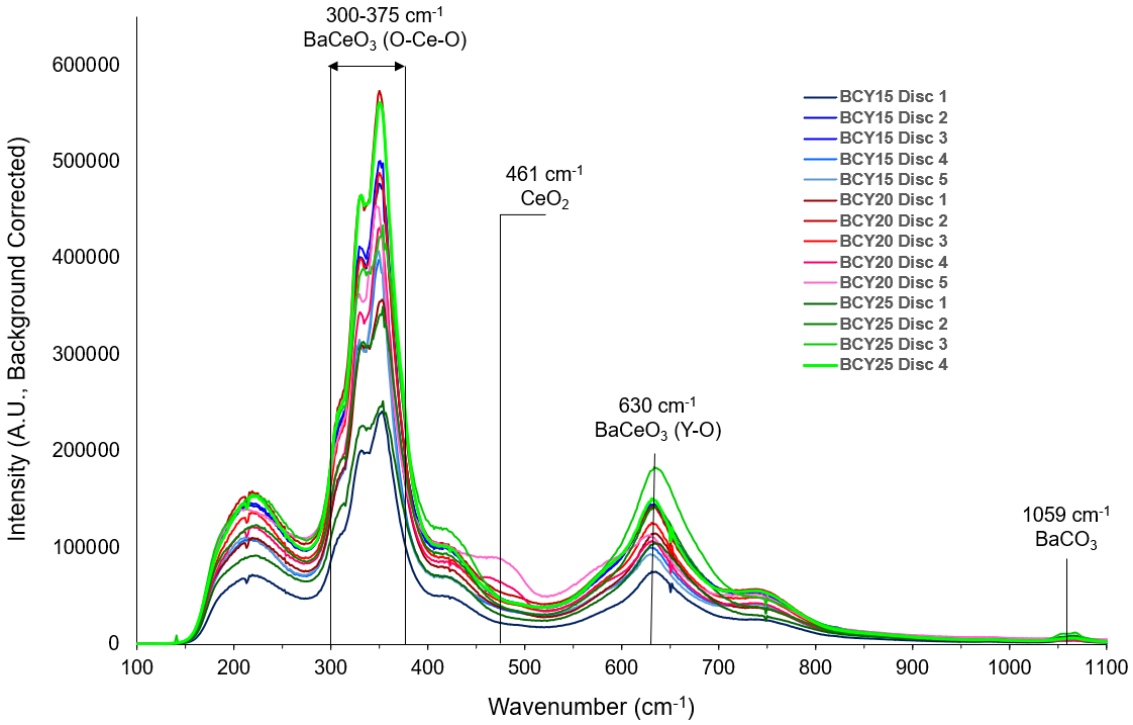

Figure 7. Raman spectra of BCY15 ($BaCe_{0.85}Y_{0.15}O_{3-\delta}$), BCY20 ($BaCe_{0.8}Y_{0.2}O_{3-\delta}$), and BCY25 ($BaCe_{0.75}Y_{0.25}O_{3-\delta}$). All spectra obtained at room temperature.

Comparing the O-Ce-O bending region for each level of dopant concentration, as demonstrated in figure 8, results in increased intensity at approximately 338 cm^{-1}. This appears to be the only noticeable change in the spectrum as Y concentration increases, suggesting that this band forms as the result of a Y-O stretch or a O-Y-O bend.

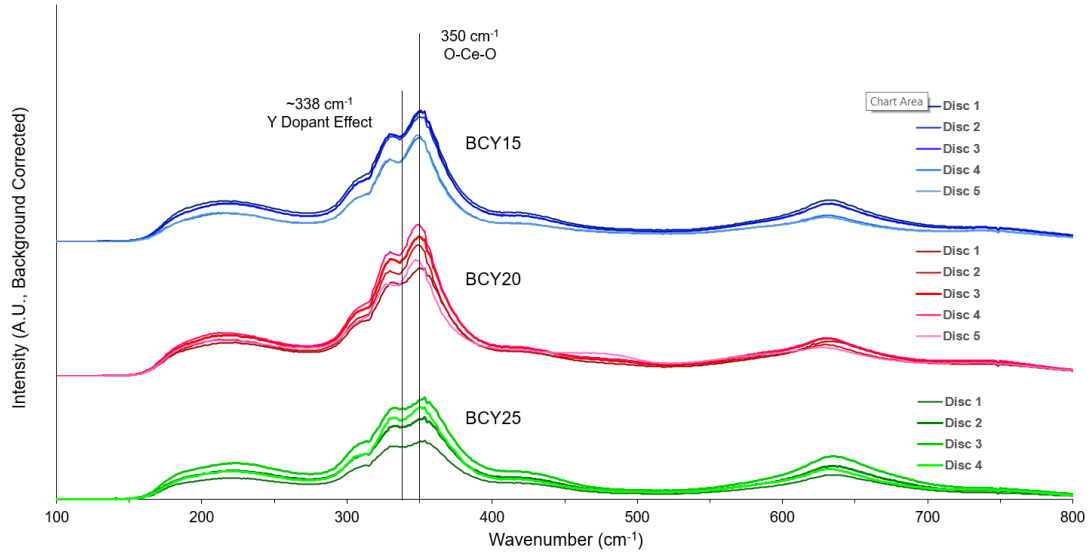

Figure 8. Raman spectra of BCYx (x = 15, 20, 25) organized according to Y^{3+} concentration to elucidate dopant effects on O-Ce-O bending region (300 cm^{-1} – 375 cm^{-1}). All spectra obtained at room temperature.

To explore long-term stability of the sintered perovskite discs, five samples of BCY20 were stored in a desiccator, while five other BCY20 samples were stored in ambient conditions. All pellets were placed in thin, 0.2 mL capacity snap-lock plastic containers. Raman spectra obtained after approximately 5 months of storage for all samples is presented in figure 9. No peak shifts were readily apparent (other than one desiccator sample which had some CeO_2 present), but the spectral intensity of the ambient storage samples was consistently lower than that of the desiccator samples. Though all other samples have been stored in desiccators, this supports that the prepared perovskite pellets were fairly resistant to degradation from water vapor and CO2 in ambient conditions.

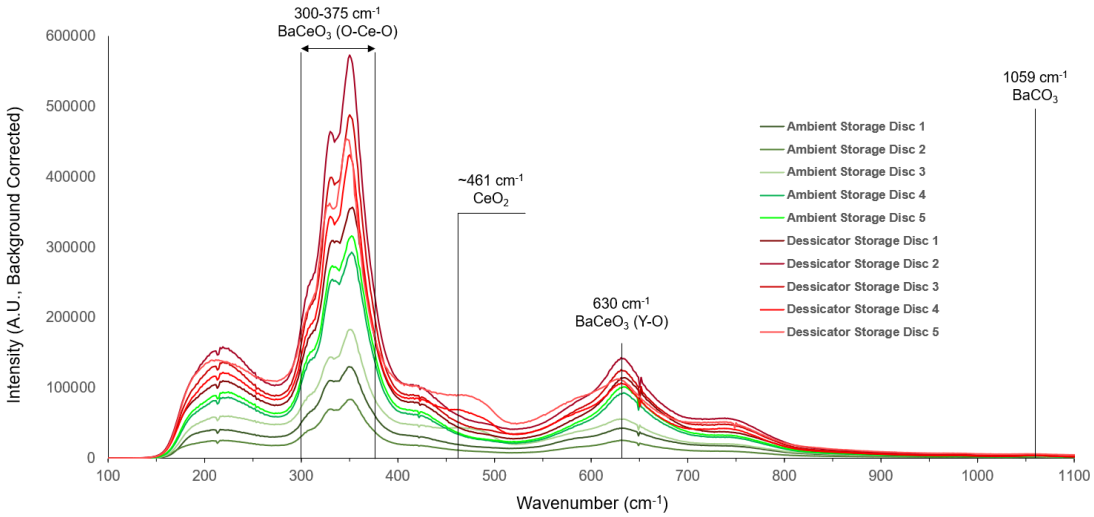

Figure 9. Raman spectra of 10 samples of BCY20, five stored in ambient conditions (green) and five stored in a desiccator filled with anhydrous $CaSO_4$ (red).

Interestingly, for each of the aforementioned perovskite disc samples, analysis of the higher wavenumber region for all spectra revealed three adjacent peaks reminiscent of ethanol, as

demonstrated in figure 10 and figure 11. This could suggest that ethanol from the binding agent solution becomes trapped during compaction and is not expelled from the lattice during sintering. However, since each peak here is shifted ~100 cm-1 upward of what has been previously reported,[25-26] additional samples must be tested to verify the validity of this claim.

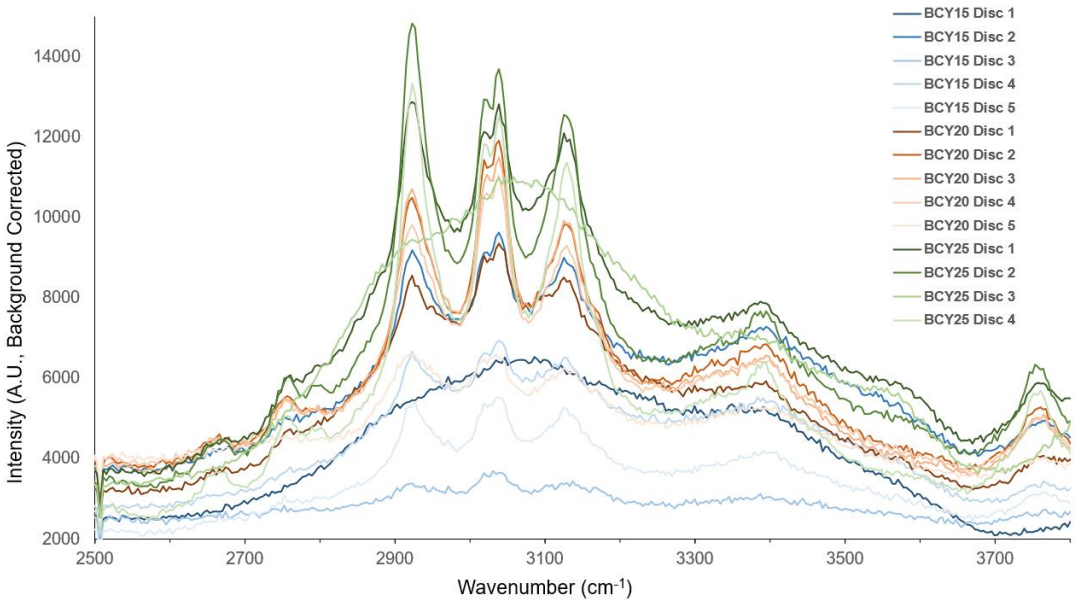

Figure 10. Raman spectra of BCY15, BCY20, and BCY25 in the high wavenumber region. All spectra obtained at room temperature.

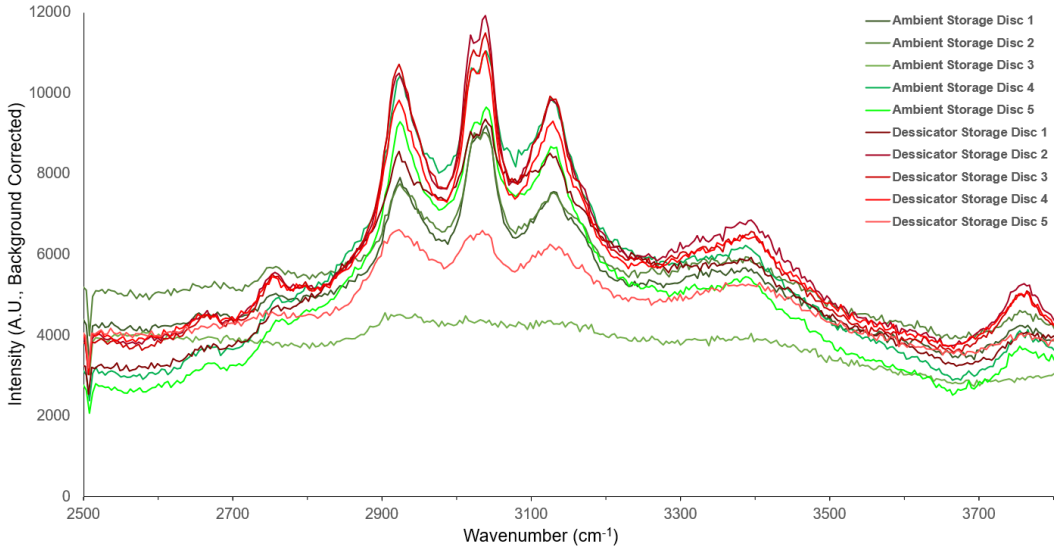

Figure 11. Raman spectra of BCY20 samples stored in ambient conditions (green) and BCY20 samples stored in a desiccator (red) in the high wavenumber region. All spectra obtained at room temperature.

As a preliminary test of perovskite hydration via exposure to liquid H_2O, a BCY20 sample was submerged in a beaker of deionized H_2O for varying lengths of time and, after each exposure to room temperature water, a Raman spectrum was acquired. The hydration was cumulative, with the perovskite discs being cleared of external water droplets using an air line between each timed

submergence step. The bending and stretching modes of the BCY20 structure, along with the typical impurity peaks found in sol-gel perovskites, were inconsistent, as demonstrated in figure 12a. The O-Ce-O stretch at 350 cm^{-1} remained fairly constant, while the CeO_2 peak at 461 cm^{-1} and unknown peak at ~600 cm^{-1}, possibly resulting from perturbation of oxide bonding upon hydration,[27] decreased from the dry sample at 5 s and 30 s of submergence in DI H_2O, but increased when the same perovskite disc was hydrated for 2 min. and 5 min. by the same method. At the same time, the $BaCO_3$ peak, which was expected to increase with additional exposure to H_2O, had a greater intensity at 5 s and 30 s of hydration than it did at 2 min. and 5 min. of liquid water exposure. To eliminate inconsistencies resulting from repeated submergence of the perovskite and re-positioning on the Raman stage to acquire each spectrum, a purpose-built cell that can be mounted under the Raman microscope and feed vapor-phase H_2O to perovskite samples is currently being designed. However, even this crude submergence test does still reveal the emergence of a peak at ~2915 cm^{-1} and a broad band centered around 3430 cm^{-1}, both of which are absent from the dry sample spectrum. The latter of these peaks is expected to result from water,[28-29] and the apparent increase with duration of submergence supports that the broad 3430 cm^{-1} peak can be correlated directly to perovskite hydration.[30]

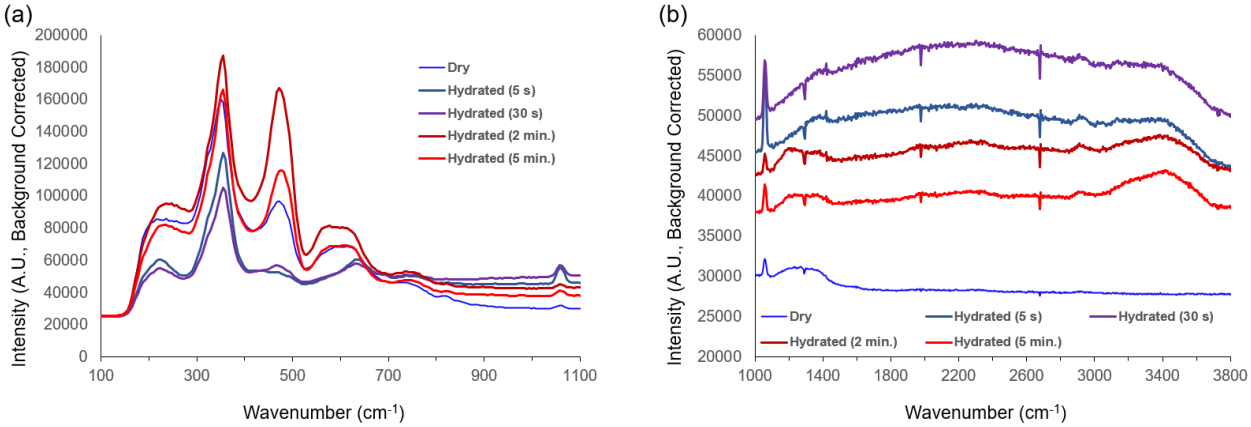

Figure 12. Raman spectra of the stretching and bending region for the BCY20 perovskite structure (a) and the expected hydration region for the same BCY20 sample (b). The single BCY20 disc was submerged in room temperature deionized H_2O for the listed times prior to acquisition of each Raman spectrum. All spectra acquired at room temperature.

Electrochemical Reactor System

Design for the reactor was inspired by polymer electrolyte membrane fuel cells, with adaptations made to permit higher temperature operation and facilitate use of a rigid, disc-shaped solid oxide electrolyte. The reactor design, illustrated as an exploded view in figure 13, is primarily comprised of stainless steel and copper current collector plates, two graphite flow field blocks, Pd-coated carbon paper GDLs, a silicone gasket, the perovskite, and four inlet/outlet graphite tubes. Graphite tubes are threaded directly into the graphite flow field blocks, with a perfluoroelastomer (FFKM) o-ring providing the seal between each part. Two additional FFKM o-rings were placed in wells surrounding each circular flow field in the middle of each block to provide a seal between each flow field and the perovskite. The silicone gasket provides a secondary seal to retain any gases that leak out of the partially porous perovskite sample. Each bolt in the system is torqued to 40 in.-lbs. All graphite components were pyrolytically sealed to prevent escape of gasses from the system via permeation through pores in the graphite.

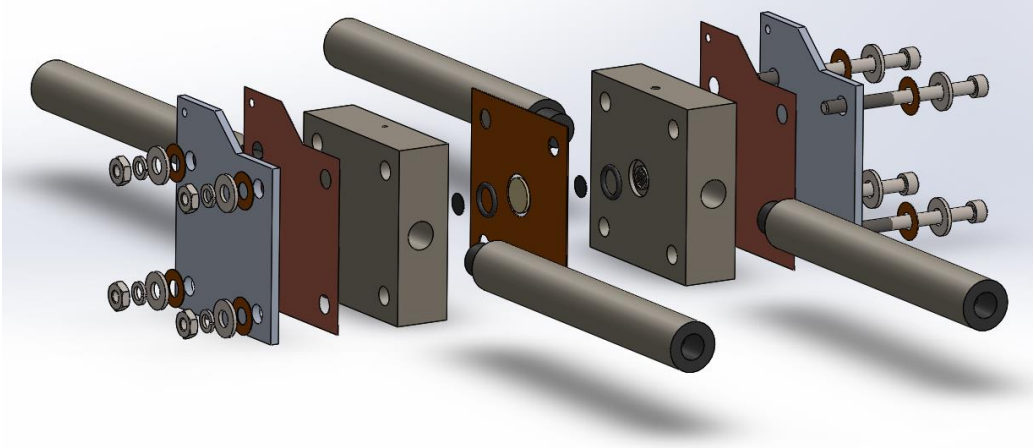

Figure 13. Exploded view of the reactor assembly. Designed in SolidWorks.

Graphite inlet/outlet tubes were implemented into the assembled reactor system (Fig. 14) to permit the use of perfluoroalkoxy alkane (PFA) unions for attaching gas lines to the cell. PFA unions were chosen because brass and stainless-steel unions present the risk of cracking the bipolar graphite flow field blocks as reactor temperature increases, since the metals experience greater thermal expansion than the graphite. PFA, however, undergoes thermal degradation above 204 °C. Therefore, graphite tubes permit the reactor to be enclosed in a chamber insulated with alumina silicate ceramic insulation to maintain stable operating temperatures between 200 °C and 300 °C while leaving the PFA outside of this chamber to be cooled naturally by natural convection or, if need be, via forced convection.

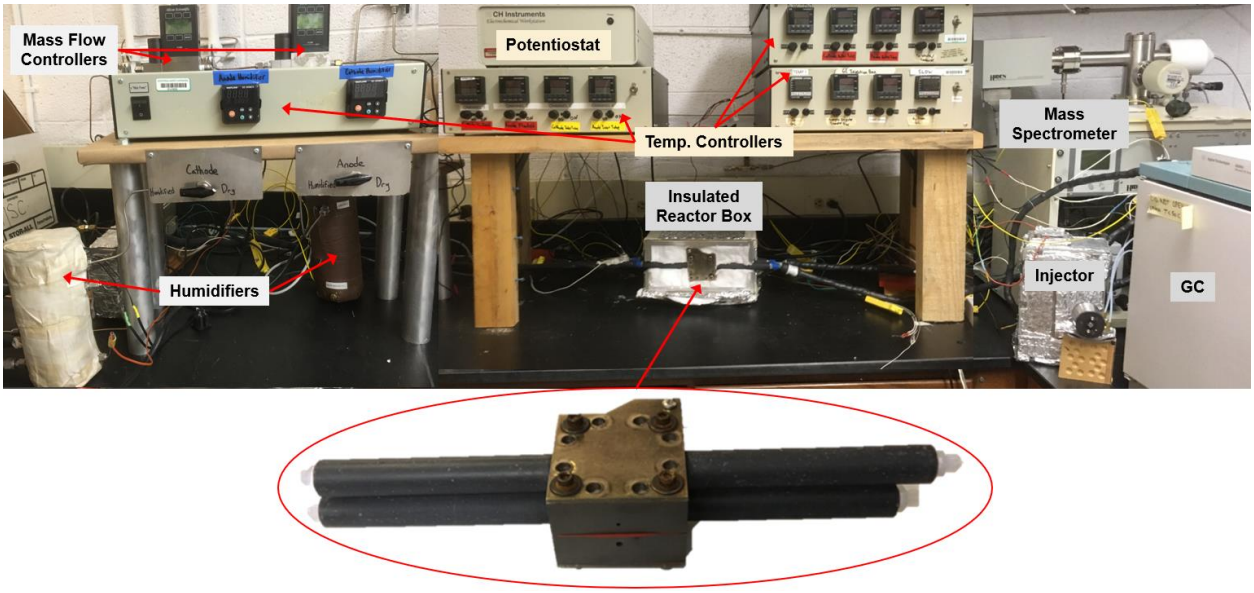

Figure 14. Full electrochemical reactor system. The inset at the bottom shows the fully assembled electrochemical reactor.

A full schematic of the entire analytical system is depicted in figure 15. Pressure of humidified H_2—delivered to the anode via mass flow controller—is controllable via a back-pressure regulator. MCH reagent is delivered by twin ISCO Teledyne tower pumps, which accurately control flow rate, to a flash evaporator before flowing through a humidifier and entering the

cathode. Cathode exhaust flows to a 6-position valve that is actuated by a separate N_2 source; actuation of the valve from load to inject is controlled by GC electronic valve operation. After analytes pass through the column, a splitter sends half of the analyte to the flame ionization detector of the GC, while the other half is sent to an open-split capillary device.[31-32] Flow rate of analyte sent to the open-split device can be precisely controlled by mass flow controller to ensure MS is not overloaded with analyte. Finally, a condenser column is placed along the GC-MS heated transfer line to capture separated liquid products if desired for further investigation by FT-IR or ^{1}H-NMR.

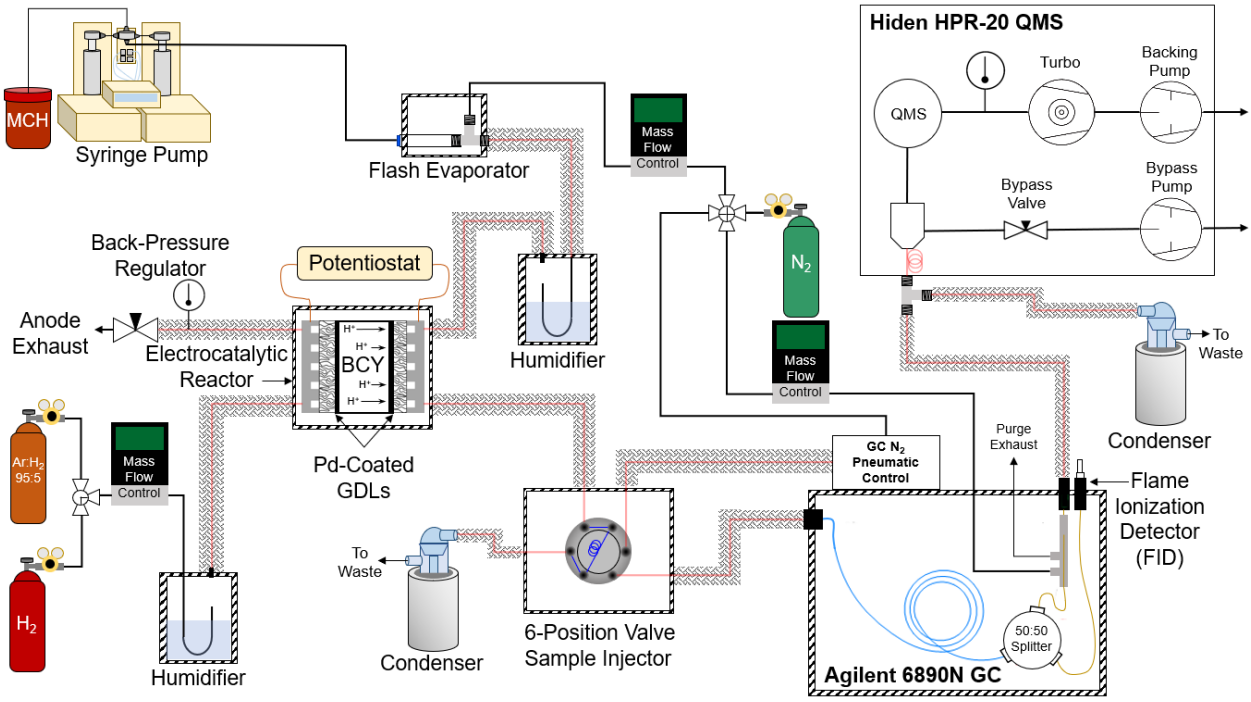

Figure 15. Analytical system for delivering reagents to and quantifying non-Faradaic products from the perovskite-based electrochemical reactor. All black lines represent uninsulated tubing, while all red lines with a white cross-link overlay represent heated transfer lines. All components surrounded by black and white striped lines are temperature-controlled.

With the most recent version of the electrochemical reactor now fully capable of preventing any leaks of reagent gases, humidified H_2 and MCH can be safely and effectively delivered to the reactor to probe the NEMCA effect. The ultimate goal remains control of the proton flux and, similarly, catalyst acidity and capacity to isomerize MCH to yield non-Faradaic products at the cathode by tuning cell potential (Fig. 15). Distributions of isomer products are expected to vary with potential. Increased proton flux through the perovskite electrolyte is predicted to yield isomers with less stable transition states, similar to the effect observed by ExxonMobil when they used zeolites with varied acidities.[11]Protons are expected to catalyze multiple isomerization prior to reductive elimination, thereby mimicking the gain observed upon increasing base current in an electrical transistor (Fig. 16, top left).

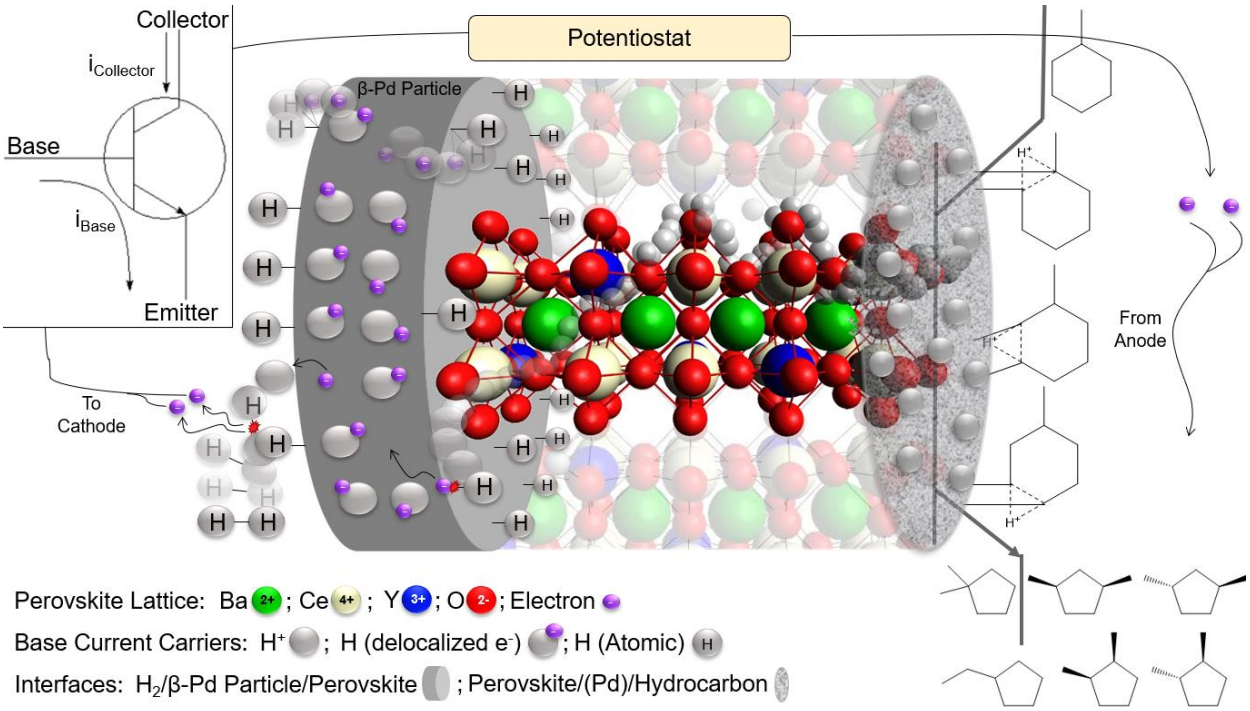

Figure 16. Schematized view of proton generation at the anode, proton conduction via the hydrated BCYx perovskite, and catalytic proton availability at the cathode interface governed by toe applied potential. Note the updated intermediate species at the cathode, whose bridgehead protons provide a more realistic prediction of intermediates compared to McVicker's cyclopropyl carbocation intermediates.

MCH Dehydrogenation Studies at Open Circuit

During the process development of the yttrium-doped barium cerate perovskite electrolytes and the prototyping phase of the reactor design, another study on MCH conversion was simultaneously carried out. Just as the NEMCA reactor uses Pd as a catalytic surface to pursue electrochemically-driven MCH isomerizations, this experiment employed another noble metal, Pt, as a catalyst for heat-generated MCH dehydrogenation reactions. Pt was loaded onto γ-alumina bead substrates by colleagues at UOP, LLC using a proprietary oil dropping process,[33-34] resulting in 5 categories of catalyst samples: 0.02 wt% Pt, 0.05 wt% Pt, 0.1 wt% Pt, 0.2 wt% Pt, and 1 wt% Pt, which were denoted as D, E, F, G, and H beads, respectively. Replicates of each catalyst Pt loading were then analyzed in our laser-activated membrane introduction mass spectrometry (LAMIMS) system (Fig. 17a).

Briefly, the LAMIMS system uses a pair of roughing pumps and two turbomolecular pumps (TMP) to evacuate the environment in front of a quadrupole mass analyzer (QMA), which is connected to the underside of a flow reactor manifold (Fig. 17b). A ZnSe window on the top face of the reactor facilitates laser heating of catalyst beads using the CO_2 marking laser. The flow reactor bed consists of a carbon paper bilayer which sits atop a 127 μm silicone membrane that separates the evacuated QMA region from the flow reactor. The upper carbon paper layer provides wells for positioning the bead samples, and the combined carbon paper layers dissipate heat to prevent thermal degradation of the silicone membrane as the CO_2 laser irradiates the catalyst beads (Fig. 17c). Liquid MCH reagent is delivered via syringe pump to a flash evaporator, where it is mixed with H_2. The mixed reagent gas is carried to the inlet manifold

where it diffuses through a porous frit. Heating the Pt-loaded γ-Al_2O_3 beads as reagent flows through the reactor catalyzes the dehydrogenation reaction. The silicone membrane is permeable to small organic species, permitting diffusion of toluene into the vacuum system where it is analyzed by the QMA. Details of the following experiments performed using the LAMIMS system are described by our recent publication in *Analytical Chemistry*.[35]

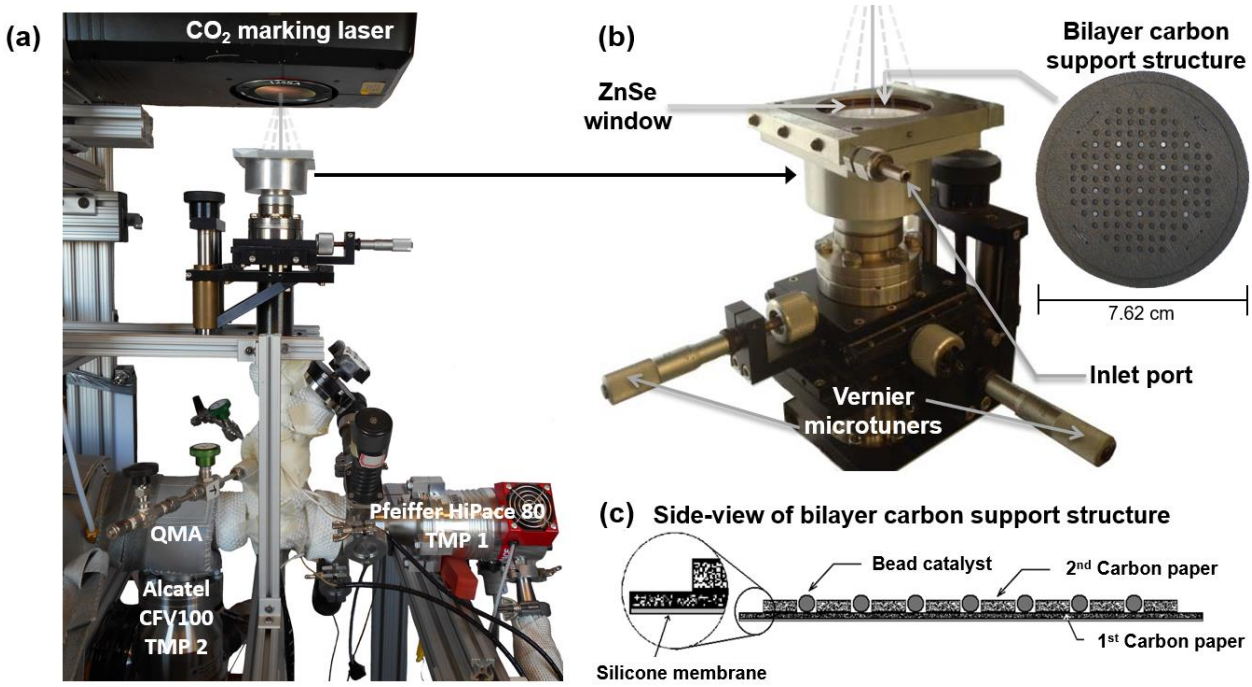

Figure 17. (a) Overview of LAMIMS system. (b) LAMIMS reactor stage. Vernier microtuners enable proper positioning of the flow reactor in the marking field of the CO_2 marking laser. A ZnSe window overlays a bilayer carbon bead support structure. (c) Cross section of the bilayer carbon bead support structure overlaying the silicone membrane separator. Image reproduced from Kim et al.[35]

Preliminary testing of the system probed for crossover signal arising from catalysts heating during irradiation of locations at 8 mm and 4 mm away from catalyst beads (Fig. 18).

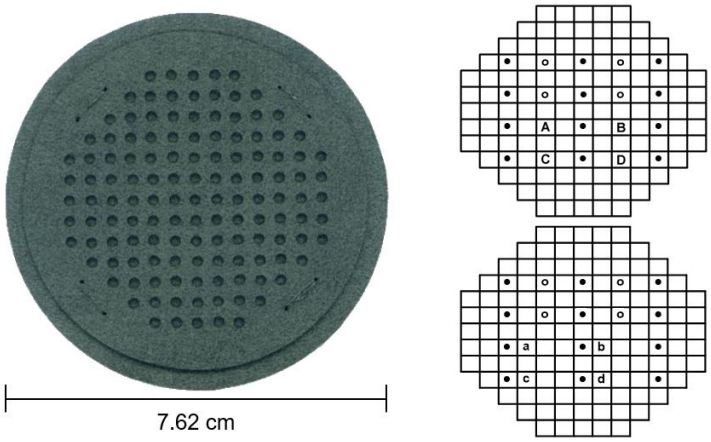

Figure 18. Carbon paper bilayer with 129 catalyst wells (left) and diagrams of sample locations for the thermal crossover study (right). E beads (●) and γ-alumina beads with no catalyst (○) were each separated by 8 mm. Top right: empty spots 8 mm from nearest E-bead (A, B, C, D). Bottom right: empty spots 4 mm from nearest E-bead (a, b, c, d).

This thermal crossover study introduced reagent at total a flow rate of 200 mL/min with MCH mole fraction (X_{MCH}) equal to 0.3. Empty spots were irradiated for 10 s at 20% of the 25-watt CO_2 laser power while QMA was monitored for toluene presence at *m/z* = 91 (Fig. 19). Empty beads (Fig. 19a and 19b) as well as beads with identical Pt loading (Fig. 19f) were also irradiated for 5 s to 10 s for comparison. Bare alumina beads surprisingly showed some minimal activity toward MCH dehydrogenation, though noticeably less so compared to the Pt-loaded beads. Irradiation of empty spots both 8 mm (Fig. 19c) and 4 mm (Fig. 19d and 19e) away from Pt-loaded beads yielded no signal, confirming that no thermal crossover is evident for beads placed in adjacent wells 4 mm apart. These results support that the carbon paper bilayer can successfully hold 129 separate bead catalyst samples with no thermal crossover effects.

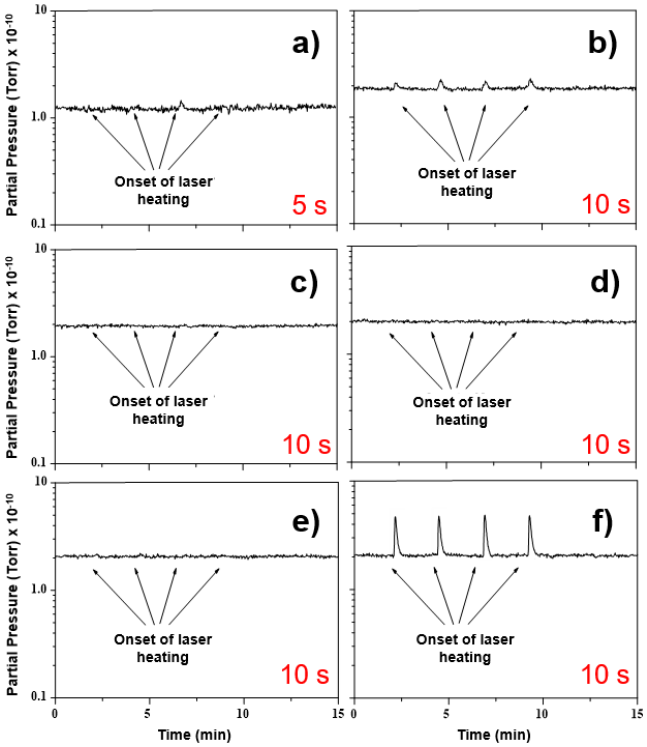

Figure 19. Toluene partial pressure from (a) four γ-Al_2O_3 beads with no Pt heated for 5 s, (b) four γ-Al_2O_3 beads with no Pt heated for 10 s, (c) four empty spots heated for 10 s at 8 mm from a catalyst bead, (d) four empty spots heated for 10 s at 4 mm from a catalyst bead, (e) empty spot a heated four consecutive times for 10 s at 4 mm from a catalyzed bead, and (f) four identically loaded Pt catalyst beads heated for 10 s. Image reproduced from Kim et al.[35]

Testing of Pt-loaded γ-alumina bead catalysts (five replicates each of D, E, F, G, and H samples) randomly positioned in the carbon paper bilayer wells initially yielded slightly inconsistent results (Fig. 20). Therefore, flow reactor uniformity was explored by sequentially irradiating 45 D-beads to probe position-dependent effects (Fig. 21). Sequential irradiation of each bead as the MCH/H_2 reagent mixture was introduced showed a clear position-dependent effect on catalytic turnover (i.e., that that samples located closer to the inlet port yielded larger toluene *m/z* peaks than samples closer to the outlet port). Therefore, modifications were made to components of the flow reactor to eliminate these effects. These modifications included increasing inlet manifold frit thickness from 0.045” to 0.14” to increase pressure drop between the inlet and flow field, increasing inlet tube diameter from 1/16” to 1/8” to minimize pressure gradient along the length of the tube, and creating an additional exhaust port on the outlet manifold. A repeat test of the 45

D catalyst beads resulted in much more consistent toluene yields from each catalyst, effectively removing the previously observed position-dependent effects. Figure 22 provides a summary of the 45 D-bead test results before and after modification.

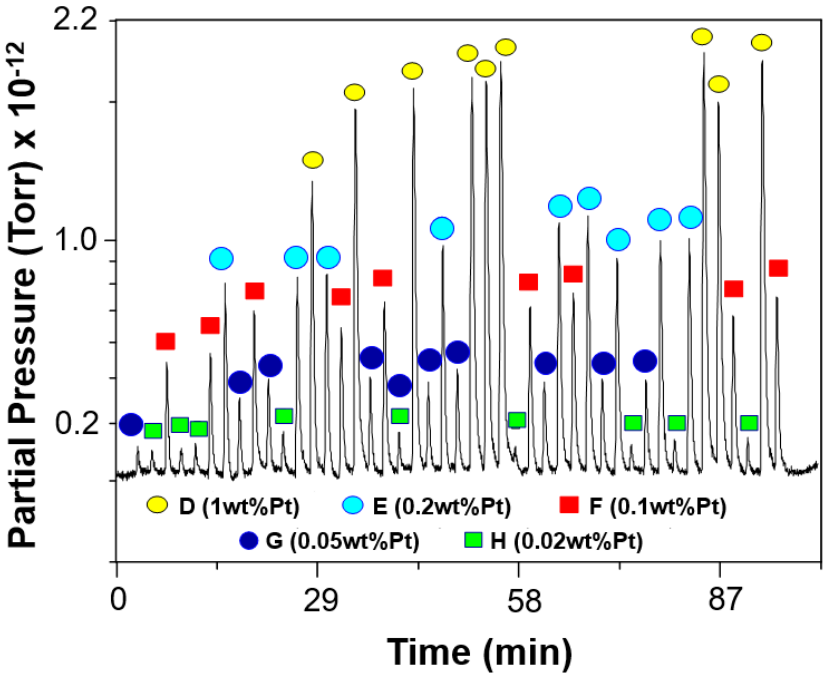

Figure 20. Toluene partial pressure from the preliminary screening of 45 Pt catalysts (nine duplicates for each of five different Pt catalysts loading). Image reproduced from Kim et al.[35]

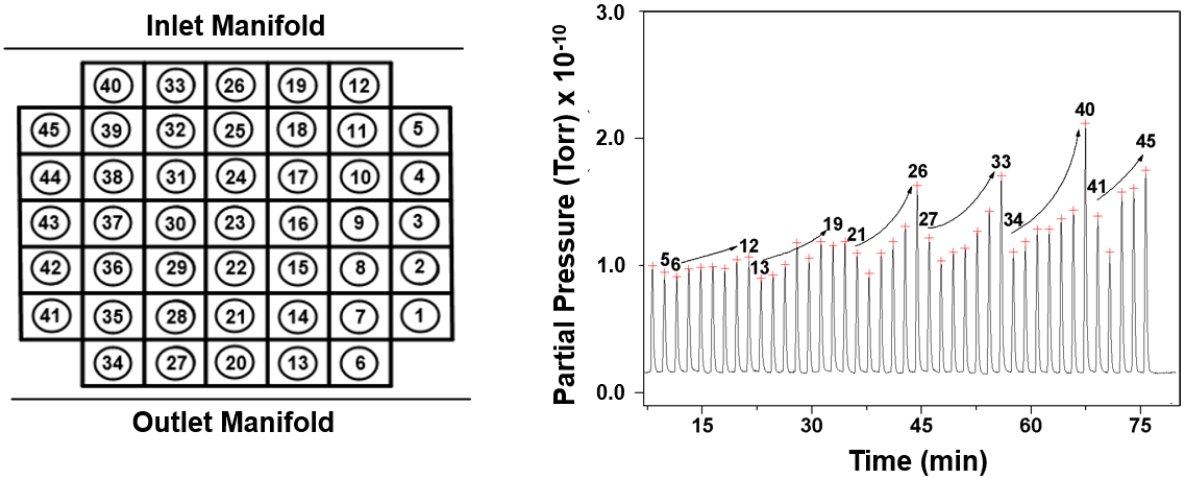

Figure 21. Left: arrangement of the forty-five catalyst D-beads; the numbers indicate the order in which the beads were irradiated by the CO_2 marking laser. Right: partial pressure monitored at *m/z* 91 as each catalyst was heated.

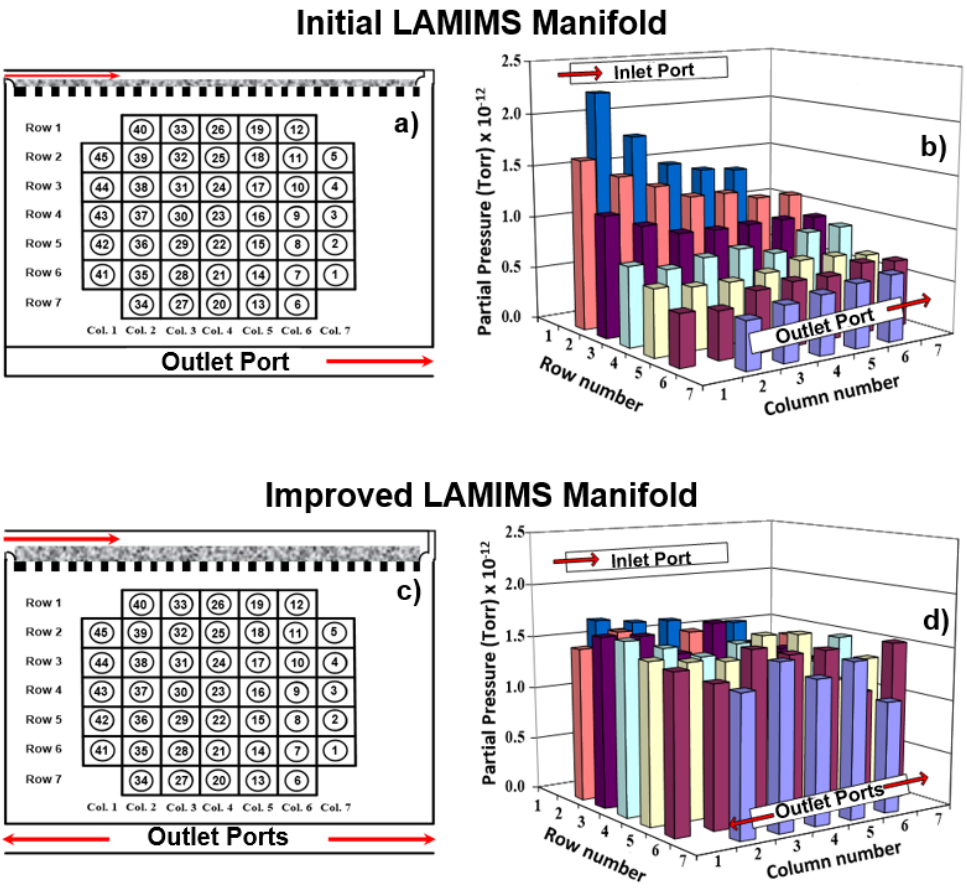

Figure 22. D bead flow uniformity study: (a) initial flow field and manifold schematic; (b) toluene partial pressures obtained from initial flow field; (c) improved manifold with thicker frit, larger inlet tube diameter, and symmetric exit ports; and (d) toluene partial pressures obtained from improved manifold. The thickness of the spotted grey bar above the catalyst arrays in (a) and (c) is proportional to the frit thickness in each test. Red arrows schematize entry and exit flow directions. Image reproduced from Kim et al.[35]

With the improvements in flow and signal uniformity brought about by the manifold modifications, the full range of Pt-loaded γ-Al_2O_3 beads were able to be more effectively investigated. D, E, F, G, and H catalyst beads (with 9 replicates of each of these 5 Pt-loadings) were once again distributed randomly among the 129 well positions of the carbon paper bilayer (Fig. 23a). Beads were first reduced by feeding pure H_2 (30 mL/min for 5 min) to the reactor while irradiating beats at 8% laser power. MCH was then delivered via tower syringe pump (Teledyne ISCO, Lincoln, NE) to a flash evaporator (heated to 115 °C). The flash evaporator was co-fed with H_2 to act as a carrier gas and to create a 200 mL/min feed stream with XMCH = 0.1. Catalyst beads were then sequentially irradiated for 5 s each while monitoring *m/z* = 91 on the QMA. Extent of dehydrogenation increased with increasing Pt loading as expected, but the actual relationship between Pt loading % and partial pressure of toluene generated was found to be logarithmic (Fig. 23b), where the logarithmic curve was given by $y = 7.3\times10^{-10} \ln(x) + 3.1\times10^{-9}$, with an R^2 of 0.98. The logarithmic relationship suggests a possible dependence of MCH dehydrogenation on Pt cluster active surface area or Pt cluster perimeter, both of which decrease with increased Pt loading as cluster overlap becomes more prominent. Surface area and perimeter have been cited as critical in standard steam reforming and electric field steam reforming, respectively, of methane over a similar Pd-CeO_2 system.[36] Furthermore, the perimeter

effect could also suggest that the Pt-substrate interface may also be crucial in the dehydrogenation mechanism, which has not been thoroughly addressed in mechanistic-specific studies.[37-38]

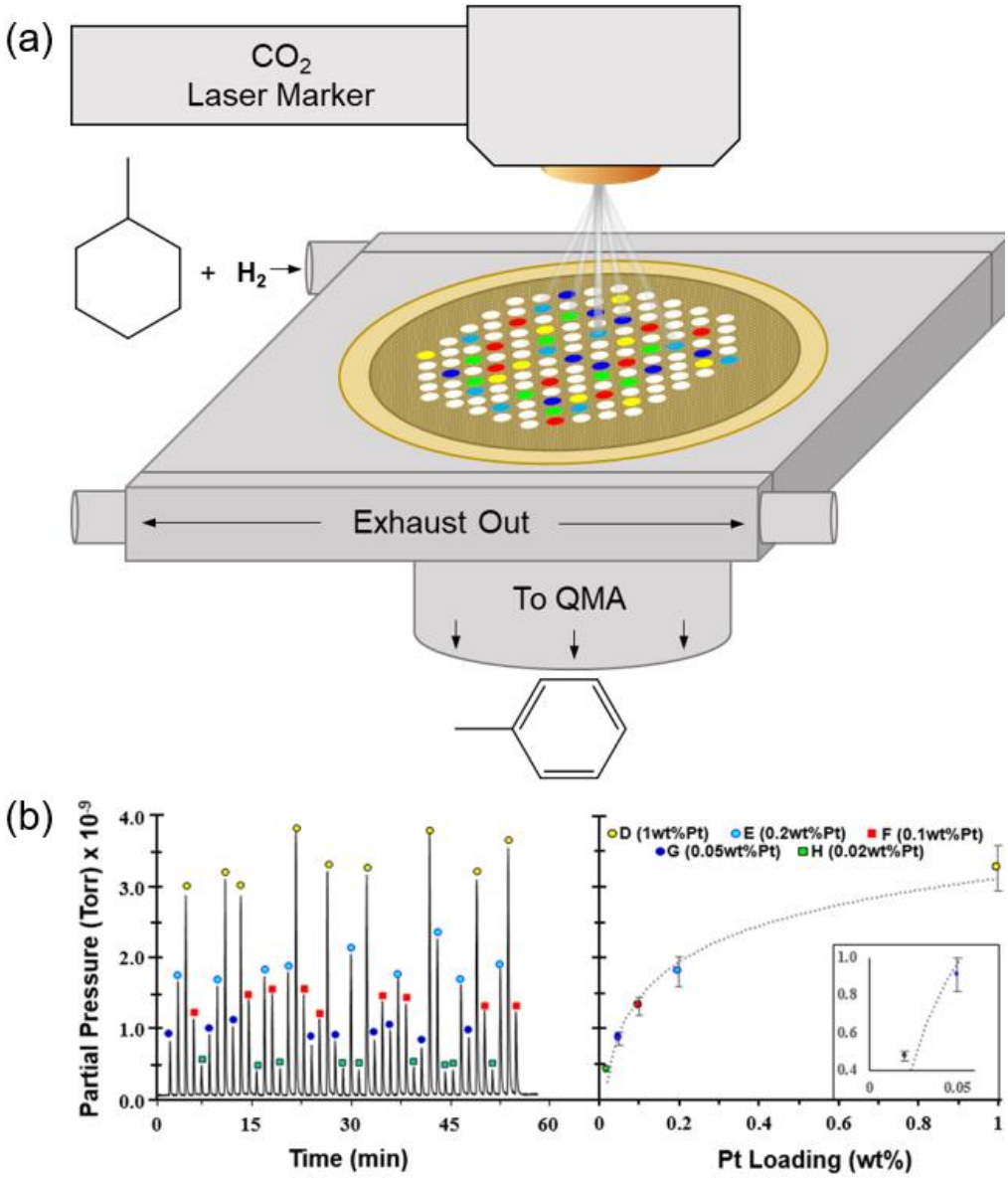

Figure 23. Schematic of the operation of the LAMIMS system during the final Pt-loaded γ-Al_2O_3 beads investigation (a) and the resulting toluene partial pressure analysis for each set of beads (b). Images reproduced from Kim et al.[35]

Recent work by Sekine and coworkers explored the dependence of MCH dehydrogenation over Pt/CeO_2 and Pt/TiO_2 on H_2 partial pressure, with and without an electric field applied to the system.[39-40] In their work, they posited that the substrates permit proton conductivity that shuttles protons from the substrate surface to the noble metal catalyst surface. Furthermore, they suggest that during dehydrogenation, a C_7H_{13}-H-H^+ intermediate forms, where an interaction occurs between an MCH ring hydrogen and a proton that has migrated to the Pt surface. The interaction results in liberation of these interacting H species as H_2. The authors do not specify a mechanism

for each individual dehydrogenation, instead suggesting that this process repeats until toluene is formed, which is eventually desorbed from the surface (Fig. 24). Coupling Sekine's observations with our results enabled us to further speculate on the exact mechanism (Fig. 25) of the dehydrogenation. Spillover H_2 generated from interaction of the feed gas H_2 with the Pt yields protons on the platinum surface. Surface protons then interact with the MCH protons to form a C-$H^{\delta-}\cdots H^{\delta+}$-Pt intermediate and liberate H_2 in the manner presented by Takise et al.[39-40] Removal of the hydride from the ring yields a carbocation that then binds with the Pt surface. After this process is completed one additional time with the adsorbed MCH species to form an adsorbed carbocation, the electrons from the MCH-Pt bond are relocated to the p-orbitals of the ring to form methylcyclohexene. This H_2 evolution process through hydride-proton pairing then continues until toluene is formed, which is eventually desorbed from the Pt surface.

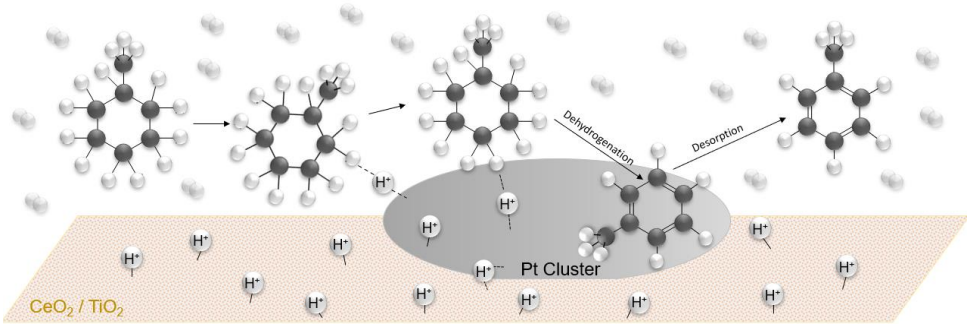

Figure 24. Dehydrogenation of MCH over a Pt/solid oxide substrate through a series of C-H-H^+ intermediates. Toluene is then desorbed from the Pt surface. Image adapted from Takise et al.[39-40]

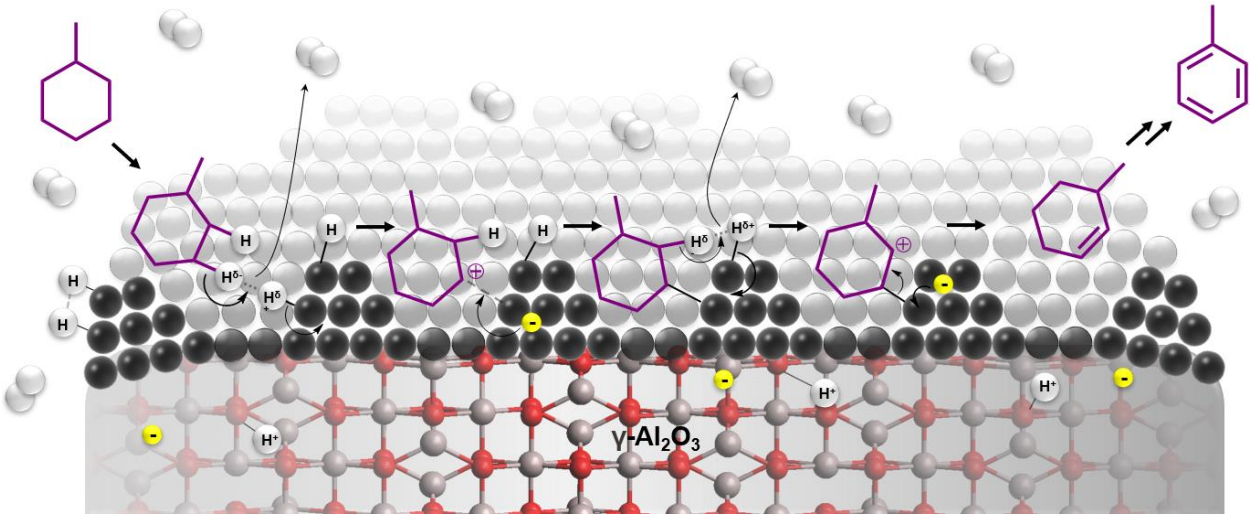

Figure 25. MCH dehydrogenation on platinized γ-alumina. Dihydrogen (white spheres) dissociates to spillover hydrogen. MCH sheds hydrides that associate with spillover protons, leaving an electron (yellow sphere) in the metal lattice (black spheres) that charge balances an adsorbed carbocation. Repetition of the process yields toluene. Image reproduced from Kim et al.[35]

Future Work

Hydration of the doped perovskites is critical to their capacity to act as proton conductors. Further understanding of the hydration dynamics, therefore, could enable a much more precisely

timed conditioning phase of system operation with respect to exposing the perovskite to humidified gases to hydrate the electrolyte. This would also aid in preserving the longevity and stability of perovskite samples, since prolonged hydration can cause formation of $BaCO_3$ and CeO_2 over time, weakening the structural integrity and decreasing proton conductivity. A more thorough understanding of temperature and time required to fully dehydrate the discs as a function of disc thickness would permit consistent dehydration after running experiments. Therefore, a Raman hydration cell (Fig. 26) has been designed to accurately and consistently acquire Raman spectra of perovskite samples as a humidified feed gas is fed to the underside of the sample. Confocal Raman spectroscopy will facilitate monitoring of the progress of hydration from one face of the perovskite disc to the other.

Raman investigation of hydration dynamics can also qualify the decoupled proton and oxide migration in doped perovskites (Fig. 27) that has been observed through conductivity measurements acquired during the hydration and dehydration processes.[41-42]

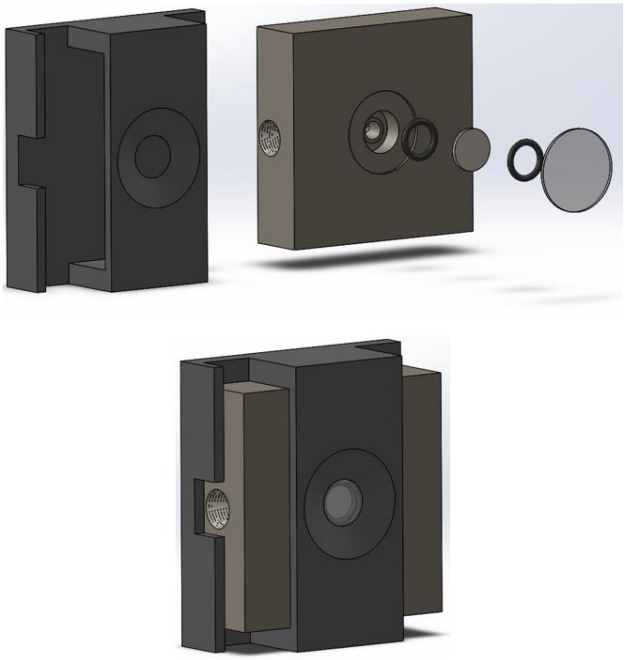

Figure 26. Exploded view (top) and fully assembled view (bottom) of a hydration cell that facilitates acquisition of Raman spectra of BCYx discs while simultaneously hydrating and heating the sample. Parts designed using SolidWorks.

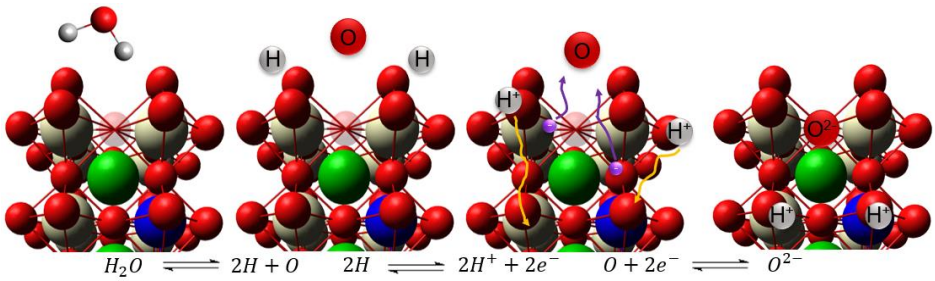

Figure 27. Uptake of H_2O by a BCY perovskite via a decoupled absorption method based on the findings of Lim et al. Colors for ion identities are identical to those in the legend of Figure 16.

Conclusion

Yttrium-doped barium cerate perovskites have been successfully synthesized and characterized. Certain structural anomalies still exist in the XRD and Raman spectra that will be addressed by modifying the synthetic workup in attempt to enhance proton conductivity and prevent porosity and grain/phase boundary formation. Analysis of catalytic activity for MCH conversion using the high-throughput LAMIMS system has demonstrated an extremely efficient manner by which catalyst activity can be measured. Simple adjustment of the upper layer of the carbon paper bilayer would easily permit the use of the thin pellet perovskite electrolytes to be directly evaluated by this system. A wider range of dopant concentrations could be employed and rapidly analyzed to determine the catalyst constitution that yields the highest degree of proton activity toward dehydrogenation, which is expected to simultaneously enhance sensitivity of proton flux for the NEMCA isomerization reactions.

Ultimately, insight gained from this study, especially if catalytic rate can be effectively enhanced by applied potential according to the NEMCA effect, would undoubtedly prove extremely valuable to numerous industries. The petrochemical industry could use this technique for more efficient conversion of crude oils to various fuels, the pharmaceutical industry could apply this electrochemical isomerization for creating difficult isomers as precursors in natural product synthesis, and those in the organic, electrochemical, and computational fields could use our results to further investigate the exact mechanism through which the isomerization occurs. We are confident that our efforts to isomerize MCH in an electrochemical reactor will yield extremely informative data relating to alkane isomerization and the NEMCA effect as a whole.

References

1. Vayenas, C. G.; Bebelis, S.; Neophytides, S., Non-Faradaic Electrochemical Modification of Catalytic Activity. *J. Phys. Chem.* **1988,** *92,* 5083-5085.
2. Levia, E. P. M., On the work function changes and other properties of the gas-exposed electrode surface in the NEMCA effect. *Top. Catal.* **2007,** *44* (3), 347-354.
3. Vayenas, C. G.; Bebelis, S. I., Electrochemical promotion. *Solid State Ion.* **1997,** *94,* 267-277.
4. de Lucas-Consuegra, A.; Dorado, F.; Valverde, J. L.; Karoum, R.; Vernoux, P., Low-temperature propene combustion over Pt/K-βAl_2O_3 electrochemical catalyst: Characterization, catalytic activity measurements, and investigation of the NEMCA effect. *J. Catal.* **2007,** *251,* 474-484.
5. Bebelis, S.; Kotsionopoulos, N., Non-faradaic electrochemical modification of the catalytic activity for propane combustion of Pt/YSZ and Rh/YSZ catalyst-electrodes. *Solid State Ion.* **2006,** *177,* 2205-2209.
6. Poulidi, D.; Thursfield, A.; Metcalfe, I. S., Electrochemical promotion of catalysis controlled by chemical potential difference across a mixed ionic-electronic conducting ceramic membrane – an example of wireless NEMCA. *Top. Catal.* **2007,** *44* (3), 435-449.
7. Bumroongsakulsawat, P.; Yindee, S.; Vanalabhpatana, P.; Assabumrungrat, S., High Faradaic Yields of Non-Faradaic Electrochemical Modification of Catalytic Activity of Propane Oxidation at Pt-YSZ. *J. Electrochem. Soc.* **2016,** *163* (13), E341-E343.

8. Ploense, L.; Salazar, M.; Gurau, B.; Smotkin, E. S., Proton Spillover Promoted Isomerization of n-Butylenes on Pd-Black Cathodes/Nafion 117. *J. Am. Chem. Soc.* **1997,** *119*, 11550-11551.
9. Ploense, L.; Salazar, M.; Gurau, B.; Smotkin, E. S., Spectroscopic study of NEMCA promoted alkene isomerizations at PEM fuel cell Pd–Nafion cathodes. *Solid State Ion.* **2000,** *136-137*, 713-720.
10. Salazar, M.; Smotkin, E. S., Electrochemically promoted olefin isomerization reactions at polymer electrolyte fuel cell membrane electrode assemblies. *J. Appl. Electrochem.* **2006,** *36* (11), 1237-1240.
11. McVicker, G. B.; Feeley, O. C.; Ziemiak, J. J.; Vaughan, D. E. W.; Strohmaier, K. C.; Kliewer, W. R.; Leta, D. P., Methylcyclohexane Ring-Contraction: A Sensitive Solid Acidity and Shape Selectivity Probe Reaction. *J. Phys. Chem.* **2005,** *109*, 2222-2226.
12. Sawant, P.; Varma, S.; Wani, B. N.; Bharadwaj, S. R., Influence of synthesis route on morphology and conduction behavior of $BaCe_{0.8}Y_{0.2}O_{3-\delta}$. *J. Therm. Anal. Calorim.* **2012,** *107*, 189-195.
13. Kulkarni, S.; Duttagupta, S.; Phatak, G., Sol–gel synthesis and protonic conductivity of yttrium doped barium cerate. *J. Sol-Gel Sci. Technol.* **2015,** *74*, 94-102.
14. Subramaniyan, A.; Tong, J.; O'Hayre, R.; Sammes, N. M., Sintering Studies on 20 mol% Yttrium-Doped Barium Cerate. *J. Am. Ceram. Soc.* **2011,** *94* (6), 1800-1804.
15. Lee, K.-R.; Tseng, C.-J.; Chang, J.-K.; Wang, K.-W.; Huang, Y.-S.; Chou, T.-C.; Chiu, K.-C.; Tsai, L.-D.; Lee, S.-W., $Ba_{1-x}Sr_xCe_{0.8-y}Zr_yY_{0.2}O_{3-\delta}$ protonic electrolytes synthesized by hetero-composition-exchange method for solid oxide fuel cells. *Int. J. Hydrogen Energy* **2017,** *42*, 22222-22227.
16. Jhuang, J.-W.; Lee, K.-R.; Chang, J.-K.; Shen, C.-T.; Lee, Y.-H.; Lee, S.-W.; Tseng, C.-J., Chemical stability and electrical and mechanical properties of $BaZr_xCe_{0.8-x}Y_{0.2}O_3$ with CeO_2 protection method. *Int. J. Hydrogen Energy* **2017,** *42*, 22259-22265.
17. Shi, Z.; Sun, W.; Wang, Z.; Qian, J.; Liu, W., Samarium and Yttrium Codoped $BaCeO_3$ Proton Conductor with Improved Sinterability and Higher Electrical Conductivity. *ACS Appl. Mater. Interfaces* **2014,** *6*, 5175-5182.
18. Zuo, C.; Zha, S.; Liu, M.; Hatano, M.; Uchiyama, M., $Ba(Zr_{0.1}Ce_{0.7}Y_{0.2})O_{3-\delta}$ as an Electrolyte for Low-Temperature Solid-Oxide Fuel Cells. *Adv. Mater.* **2006,** *18*, 3318-3320.
19. Ubic, R., Revised Method for the Prediction of Lattice Constants in Cubic and Pseudocubic Perovskites. *J. Am. Ceram. Soc.* **2007,** *90* (10), 3326-3330.
20. Tu, C.-S.; Chien, R. R.; Schmidt, V. H.; Lee, S.-C.; Huang, C.-C.; Tsai, C.-L., Thermal stability of $Ba(Zr_{0.8-x}Ce_xY_{0.2})O_{2.9}$ ceramics in carbon dioxide. *J. Appl. Phys.* **2009,** *105*, 103504.
21. Scherban, T.; Villeneuve, R.; Abello, L.; Lucazeau, G., Raman scattering study of acceptor-doped $BaCeO_3$. *Solid State Ion.* **1993,** *61*, 93-98.
22. Slodczyk, A.; Sharp, M. D.; Upasen, S.; Colomban, P.; Kilner, J. A., Combined bulk and surface analysis of the $BaCe_{0.5}Zr_{0.3}Y_{0.16}Zn_{0.04}O_{3-\delta}$ (BCZYZ) ceramic proton-conducting electrolyte. *Solid State Ion.* **2014,** *262*, 870-874.
23. Loridant, S.; Abello, L.; Siebert, E.; Lucazeau, G., Correlations between structural and electrical properties of $BaCeO_3$ studied by coupled in-situ Raman scattering and impedance spectroscopy. *Solid State Ion.* **1995,** *78*, 249-258.

24. Kannan, R.; Gill, S.; Maffei, N.; Thangadurai, V., $BaCe_{0.85-x}Zr_xSm_{0.15}O_{3-\delta}$ ($0.01 < x < 0.3$) (BCZS): Effect of Zr Content in BCZS on Chemical Stability in CO_2 and H_2O Vapor, and Proton Conductivity. *J. Electrochem. Soc.* **2013,** *160* (1), F18-F26.
25. Yu, Y.; Lin, K.; Zhou, X.; Wang, H.; Liu, S.; Ma, X., New C-H Stretching Vibrational Spectral Features in the Raman Spectra of Gaseous and Liquid Ethanol. *J. Phys. Chem. C* **2007,** *111*, 8971-8978.
26. Mammone, J. F.; Sharma, S. K.; Nicol, M., Raman Spectra of Methanol and Ethanol at Pressures up to 100 kbar. *J. Phys. Chem.* **1980,** *84*, 3130-3134.
27. Karlsson, M.; Matic, A.; Knee, C. S.; Ahmed, I.; Eriksson, S.; Börjesson, L., Short-Range Structure of Proton-Conducting Perovskite $BaIn_xZr_{1-x}O_{3-x/2}$ ($x = 0$-0.75). *Chem. Mater.* **2008,** *20*, 3480-3486.
28. Hu, Q.; Zhao, H.; Ouyang, S., Understanding water structure from Raman spectra of isotopic substitution H_2O/D_2O up to 573 K. *Phys. Chem. Chem. Phys.* **2017,** *19*, 21540-21547.
29. Auer, B. M.; Skinner, J. L., IR and Raman spectra of liquid water: Theory and interpretation. *J. Chem. Phys.* **2008,** *128*, 224511.
30. Bielecki, J.; Parker, S. F.; Mazzei, L.; Börjesson, L.; Karlsson, M., Structure and dehydration mechanism of the proton conducting oxide $Ba_2In_2O_5(H_2O)_x$. *J. Mater. Chem. A* **2016,** *4*, 1224-1232.
31. Davies, N. W., Open split interfaces in capillary gas chromatography-mass spectrometry: Yield and quantitative aspects. *J. Chromatogr. A* **1988,** *450*, 388-393.
32. Arrendale, R. F.; Severson, R. F.; Chortyk, O. T., Open Split Interface for Capillary Gas Chromatography/Mass Spectrometry. *Anal. Chem.* **1984,** *56*, 1533-1537.
33. Abdollahi, M.; Atashi, H.; Tabrizi, F. F., Parametric investigation of γ-alumina granule preparation via the oil-drop route. *Adv. Powder Technol.* **2017,** *28*, 1356-1371.
34. Islam, A.; Taufiq-Yap, Y. H.; Chu, C.-M.; Chan, E.-S.; Ravindra, P., Synthesis and characterization of millimetric gamma alumina spherical particles by oil drop granulation method. *J. Porous Mater.* **2012,** *19*, 807-817.
35. Kim, R. Y.; Rivera, H.; Evarts, S. E.; Rodríguez-Martínez, J. A.; Willis, R. R.; Galloway, D. B.; Falih, F.; McCall, M. J.; Smith, S. J.; Perz, K.; Smotkin, E. S., A Laser-Activated Membrane Introduction Mass Spectrometry Study of Proton Spillover Promoted Alkane Dehydrogenation. *Anal. Chem.* **2020,** *92*, 13462-13469.
36. Manabe, R.; Okada, S.; Inagaki, R.; Oshima, K.; Ogo, S.; Sekine, Y., Surface Protonics Promotes Catalysis. *Sci. Rep.* **2016,** *6*, 38007.
37. Chen, F.; Huang, Y.; Mi, C.; Wu, K.; Wang, W.; Li, W.; Yang, Y., Density functional theory study on catalytic dehydrogenation of methylcyclohexane on Pt(111). *Int. J. Hydrogen Energy* **2020,** *45*, 6727-6737.
38. Zhao, W.; Chizallet, C.; Sautet, P.; Raybaud, P., Dehydrogenation mechanisms of methyl-cyclohexane on γ-Al_2O_3 supported Pt_{13}: Impact of cluster ductility. *J. Catal.* **2019,** *370*, 118-129.
39. Takise, K.; Sato, A.; Murakami, K.; Ogo, S.; Seo, J. G.; Imagawa, K.; Kado, S.; Sekine, Y., Irreversible catalytic methylcyclohexane dehydrogenation by surface protonics at low temperature. *RSC Adv.* **2019,** *9*, 5918-5924.
40. Takise, K.; Sato, A.; Ogo, S.; Geo, J. G.; Imagawa, K.; Kado, S.; Sekine, Y., Low-temperature selective catalytic dehydrogenation of methylcyclohexane by surface protonics. *RSC Adv.* **2019,** *9*, 27743-27748.

41. Lim, D.-K.; Im, H.-N.; Song, S.-J.; Yoo, H.-I., Hydration of Proton-conducting $BaCe_{0.9}Y_{0.1}O_{3-\delta}$ by Decoupled Mass Transport. *Sci. Rep.* **2017,** *7*, 486.
42. Lim, D.-K.; Jeon, S.-Y.; Singh, B.; Park, J.-Y.; Song, S.-J., Surface exchange kinetics and chemical diffusivities of $BaZr_{0.2}Ce_{0.65}Y_{0.15}O_{3-\delta}$ by electrical conductivity relaxation. *J. Alloy. Compd.* **2014,** *610*, 301-307.